

# The role of asteroid strength, porosity and internal friction in impact momentum transfer

S.D. Raducan<sup>a,\*</sup>, T.M. Davison<sup>a</sup>, R. Luther<sup>b</sup>, G.S. Collins<sup>a</sup>

<sup>a</sup> Impacts and Astromaterials Research Centre, Department of Earth Science and Engineering, Imperial College London, SW7 2AZ, United Kingdom

<sup>b</sup> Museum für Naturkunde Berlin, Leibniz Institute for Evolution and Biodiversity Science, D-10115 Berlin, Germany

## ARTICLE INFO

### Keywords:

Impact cratering  
Ejecta  
Numerical simulations  
Asteroids  
Kinetic impactor

## ABSTRACT

Earth is continually impacted by very small asteroids and debris, and a larger object, though uncommon, could produce a severe natural hazard. During impact crater formation the ballistic ejection of material out of the crater is a major process, which holds significance for an impact study into the deflection of asteroids. In this study we numerically simulate impacts into low-gravity, strength dominated asteroid surfaces using the iSALE shock physics code, and consider the Double Asteroid Redirection Test (DART) mission as a case study. We find that target cohesion, initial porosity, and internal friction coefficient greatly influence ejecta mass/velocity/launch-position distributions and hence the amount by which an asteroid can be deflected. Our results show that as the cohesion is decreased the ratio of ejected momentum to impactor momentum,  $\beta - 1$ , increases;  $\beta - 1$  also increases as the initial porosity and internal friction coefficient of the asteroid surface decrease. Using nominal impactor parameters and reasonable estimates for the material properties of the Didymos binary asteroid, the DART target, our simulations show that the ejecta produced from the impact can enhance the deflection by a factor of 2 to 4. We use numerical impact simulations that replicate conditions in several laboratory experiments to demonstrate that our approach to quantify ejecta properties is consistent with impact experiments in analogous materials. Finally, we investigate the self-consistency between the crater size and ejection speed scaling relationships previously derived from the point-source approximation for impacts into the same target material.

## 1. Introduction

Impacts and collisions at high velocity play an important role in planetary formation and have shaped the surfaces of all solid bodies in the Solar System (Fassett and Minton, 2013). A major process during impact crater formation is the ballistic ejection of material out of the crater (Melosh, 1989). Quantifying how target properties such as strength, porosity and internal friction affect the mass-velocity distribution of ejected debris (ejecta) is important for many areas of planetary science and can help explain the evolutionary history of planetary embryos (Housen et al., 1983), the origin of interplanetary space debris (Su, 1990) and meteorites (Greenberg and Chapman, 1983) and the distribution of regolith and secondary impact craters on a planetary surface (Oberbeck, 1975; Schultz and Mendenhall, 1979). One of the most straightforward applications of ejecta studies is in the deflection of asteroids (Belton et al., 2004). To avoid a collision between an asteroid and Earth, the course of the asteroid can be changed by impacting its surface (Ahrens and Harris, 1992; Melosh et al., 1994). The ejecta

resulting from the impact can produce additional thrust which enhances the asteroid deflection (Shafer et al., 1994), but this effect has been found to vary significantly depending on the target asteroid's properties and composition (Holsapple and Housen, 2012).

An extensive number of laboratory impact experiments have been performed into various target materials (Gault et al., 1963; Hartmann, 1985; Housen, 1992; Housen and Holsapple, 2003; Housen and Holsapple, 2011; Shoemaker et al., 1963) to illuminate the ejection process and provide a quantitative measure of the mass-velocity distribution of ejected debris material. Such experiments have shown that ejecta properties are highly dependent on the target properties, in particular strength, porosity and internal friction (Holsapple and Housen, 2012; Jutzi and Michel, 2014; Michel, 2013). However, as these experiments typically do not directly replicate the low gravity, low target cohesion or large impactor sizes often involved in impacts on asteroid surfaces, their results must be extrapolated to the relevant regime using scaling theory.

Scaling relations based on the point-source approximation (Housen

\* Corresponding author.

E-mail addresses: [s.raducan16@imperial.ac.uk](mailto:s.raducan16@imperial.ac.uk) (S.D. Raducan), [thomas.davison@imperial.ac.uk](mailto:thomas.davison@imperial.ac.uk) (T.M. Davison), [robert.luther@mf.n.berlin](mailto:robert.luther@mf.n.berlin) (R. Luther), [g.collins@imperial.ac.uk](mailto:g.collins@imperial.ac.uk) (G.S. Collins).

<https://doi.org/10.1016/j.icarus.2019.03.040>

Received 28 August 2018; Received in revised form 23 January 2019; Accepted 27 March 2019

Available online 06 April 2019

0019-1035/ © 2019 Elsevier Inc. All rights reserved.

et al., 1983) provide a theoretical description of the mass/velocity/launch-position distributions of ejecta. Ejection velocity decreases with increasing launch position, following an inverse power law that breaks down close to the impact point and as it approaches the final crater rim. Recently proposed scaling relations augment the power-law relations with an empirical function to account for the reduction to zero of ejecta launch speeds near the rim (Housen and Holsapple, 2011). The current scaling relations are still not well constrained for very fast ejecta, which are also very difficult to measure in laboratory experiments. The exponent of the power-law was found to be strongly influenced by target properties (Housen et al., 1983), but these properties are interlinked and their individual influence on the ejecta needs further study.

Numerical studies using a range of initial conditions provide an alternative method to systematically determine the reaction of different types of target asteroid surfaces to a possible impact. For example, Luther et al. (2018) used numerical simulations to constrain the influence of impact velocity and target properties on ejection velocity and angles in gravity-dominated impacts. Here, we use numerical simulations of strength-dominated impacts on small, low-gravity asteroids to investigate and quantify the effects of individual asteroid surface material properties, specifically strength, porosity and internal friction, on crater ejecta properties. We use NASA's DART mission (Cheng et al., 2016; Michel et al., 2016) as a motivating case study. The paper begins with a brief summary of the DART mission, asteroid deflection by momentum transfer, and ejecta scaling relationships based on the point-source approximation and experimental ejecta measurements (Housen and Holsapple, 2011). To test the accuracy of the numerical model we first compare simulation results against laboratory experiments of vertical impacts into different types of sand, in which ejecta dynamics were measured. We then present the results of simulations of impacts into asteroid surfaces with different cohesions, porosities and internal friction coefficients and record the final crater dimensions and the mass/velocity/launch-position distribution of the resulting ejecta. These results were used to verify ejecta scaling relationships, to determine the empirical constants that define these relationships for specific material properties, and to determine the momentum transferred from the impactor to the target, which is the important metric for potential asteroid deflection.

## 2. Ejecta

### 2.1. Implications for momentum transfer and asteroid deflection

If a large asteroid were detected in advance to be on an Earth impacting trajectory, an appropriate action could be taken. Asteroid deflection methods include nuclear explosions (Ahrens and Harris, 1992), gravity tractors (Lu and Love, 2005) and kinetic impactors (Melosh et al., 1994). The latter seems to be the most straightforward solution, however a technology demonstration has yet to be implemented. NASA's proposed Double Asteroid Redirection Test (DART) mission aims to impact the smaller component of the 65803 Didymos double asteroid system, 'Didymoon', and to change its period of rotation by an amount detectable from Earth's observatories (Michel et al., 2016). DART will be the first mission to test a controlled deflection of a Near-Earth asteroid (Cheng et al., 2016). To further study the outcome of the DART impact, ESA is planning a rendezvous mission, Hera, which will arrive at the asteroid system several years after DART (Cheng et al., 2018; Michel et al., 2018). Hera will take high-resolution images of the surface and accurate measurements of the deflection, data which will allow simulations such as those presented here to be validated.

In a high velocity impact event the momentum transferred to the asteroid has two components: the momentum that is directly imparted from the impactor, and an additional momentum transferred to the target by the thrust in the opposing direction of crater ejecta that escapes the gravitational attraction of the target body.

The change in linear momentum of the asteroid as a result of the

impact,  $\Delta \mathbf{p}$ , is therefore equal to the impactor momentum  $\mathbf{p}_{imp}$  plus the resultant momentum of the escaping ejecta  $\mathbf{p}_{ej}$ . Assuming that  $\mathbf{p}_{imp}$  and  $\mathbf{p}_{ej}$  are anti-parallel, which is true for a vertical impact on a planar surface, the magnitude of the momentum change is given by:

$$\Delta p = mU + p_{ej} = \beta mU. \quad (1)$$

where  $m$  is the impactor mass and  $U$  is the impactor speed,  $p_{ej}$  is the magnitude of the ejected momentum in the opposite direction to the impact and  $\beta$  is known as the momentum multiplication factor (Housen and Holsapple, 2011)—a measure of the efficiency of momentum transfer. The ratio of ejecta momentum to the impactor momentum can also be expressed in terms of  $\beta$ ,

$$\beta - 1 = \frac{p_{ej}}{mU}. \quad (2)$$

If the ejected momentum makes no contribution to the total imparted momentum  $\beta = 1$ , and  $\beta > 2$  implies a larger contribution to the overall momentum from the crater ejecta than the impactor itself. Previous work has shown that  $\beta$  and hence the efficiency of momentum transfer in hypervelocity cratering is strongly dependent on the impact speed, the size of the asteroid, as well as its composition and structure (Cheng et al., 2016; Jutzi and Michel, 2014; Stickle et al., 2015; Syal et al., 2016).

In high velocity impacts, the ejection efficiency is an important component of the momentum transfer. The ability to predict the crater size and hence the ejecta production empirically is also important in predicting the momentum transfer.

### 2.2. Crater and ejecta scaling relationships

To aid the interpretation of our numerical simulation results and compare them with experimental data we first summarise relevant crater and ejecta scaling relationships. The outcomes of planetary cratering, such as the size of the crater and the speed and mass of ejecta, can be predicted empirically if the impactor and target properties are known (Schmidt and Holsapple, 1982). Assuming that the impact can be approximated as a point source of energy and momentum, far-field/late-stage properties of the impact can be determined by a single variable, known as the coupling parameter,  $C$  (Holsapple and Schmidt, 1987), given by

$$C = aU^\mu \delta^\nu. \quad (3)$$

The coupling parameter depends primarily on the properties of the impactor (radius  $a$ , density  $\delta$  and velocity  $U$ ). The density scaling exponent,  $\nu$ , has thus far been assumed to be independent of the material type (Housen and Holsapple, 2011) and previous experimental studies suggest  $\nu \approx 0.4$  (Schmidt, 1980). The velocity scaling exponent,  $\mu$  (often called the "velocity exponent"), however, depends on the target material properties and its value lies between two theoretical limits (Holsapple and Schmidt, 1982):  $\mu = 1/3$  if the crater formation is influenced by the impactor momentum alone or  $\mu = 2/3$  if the it is influenced by the impactor energy alone.

For known impact conditions, when considering a spherical impactor of mass  $m$  and density  $\delta$ , impacting a target of density  $\rho$  and strength  $Y$ , at a velocity  $U$ , the radius of the crater (measured at the preimpact surface),  $R$ , can be expressed in terms of the widely used dimensionless  $\pi$  scaling parameters (Holsapple, 1993). The cratering process occurs in the strength regime if the dominant resisting force to crater growth is the target's cohesive strength and in this case, the scaling parameter  $\pi_3 = \frac{Y}{\rho U^2}$  is used to express the crater radius

$$R \left( \frac{\rho}{m} \right)^{1/3} = H_2 \left( \frac{\rho}{\delta} \right)^{(1-3\nu)/3} \left( \frac{Y}{\rho U^2} \right)^{-\mu/2} \quad (\text{strength}). \quad (4)$$

On the other hand, if the weight of the excavated material dominates over cohesive strength, then the crater forms in the gravity regime and the crater radius is expressed in terms of the  $\pi_2 = \frac{ga}{U^2}$

parameter

$$R\left(\frac{\rho}{m}\right)^{1/3} = H_1\left(\frac{\rho}{\delta}\right)^{(2+\mu-6\nu)/[3(2+\mu)]}\left(\frac{ga}{U^2}\right)^{-\mu/(2+\mu)} \quad (\text{gravity}), \quad (5)$$

where  $H_1$  and  $H_2$  are constants determined from laboratory experiments. Note that in both cases, the exponent in the power-law is a function of the material-dependent velocity exponent  $\mu$ . Using the point-source approximation and dimensional analysis, Housen et al. (1983) developed a number of power-law scaling equations that relate properties of ejecta to the initial impact conditions. For instance, in one such ejecta scaling relation, the speed of ejecta normalised by the impactor velocity,  $v/U$ , is expressed as a power-law of normalised launch position,  $x/a$ , and impactor and target properties (Housen and Holsapple, 2011; Housen et al., 1983):

$$\frac{v(x)}{U} = C\left[\frac{x}{a}\left(\frac{\rho}{\delta}\right)^\nu\right]^{-\frac{1}{\mu}} \quad (6)$$

where  $\nu$  and  $\mu$  are as previously defined, and  $C$  is an empirically determined constant. However, laboratory experiments have shown that ejecta velocity distributions deviate from a simple power-law form close to the impact point and near the final crater rim. To address the deviation of ejecta scaling from a simple power law near the crater rim, where the ejection flow is increasingly affected by gravity and strength, ultimately reducing the ejection speed to zero, Housen and Holsapple (2011) proposed a simple empirical modification to Eq. (6), such that the ejection velocity drops to zero near the crater edge, at a distance proportional to the crater radius,  $R$ :

$$\frac{v(x)}{U} = C_1\left[\frac{x}{a}\left(\frac{\rho}{\delta}\right)^\nu\right]^{-\frac{1}{\mu}}\left(1 - \frac{x}{n_2R}\right)^p, \quad (7)$$

where  $C_1$  and  $p$  are constants determined by fitting the equation to empirical data. The velocity cut-off takes place at  $x = n_2R$ , where  $n_2$  is a material dependent constant, but previous studies suggest that it holds a value of approximately 1.0 (Housen and Holsapple, 2011).

The power-law also breaks down for the very fast ejecta, launched at distances  $x < n_1a$ , where  $n_1$  is a constant dependent on the projectile shape, material and impact velocity (Housen and Holsapple, 2011). The material below the impactor is driven downwards and does not get ejected, while the material close to the contact zone between the impactor and target gets ejected at very low angles, by the ‘jetting’ process (Yang and Ahrens, 1995). Due to the very high velocities involved, this process is very hard to measure in laboratory based experiments and not enough data is available.

Hermalyn and Schultz (2010) performed a series of impact experiments into sand, measuring the early-time high-speed ejecta produced by projectiles of different densities. They found that the projectile density affects the coupling time and the penetration depth. However, the current ejecta model does not account for these effects.

The ejection speed decreases as the launch distance  $x$  increases, so Housen and Holsapple (2011) also defines the mass ejected at speeds larger than  $v$ ,  $M(>v)$ , as the mass of material  $M(<x)$  launched at distances from within  $x$ , where

$$\frac{M(<x)}{m} = \frac{3k}{4\pi}\frac{\rho}{\delta}\left[\left(\frac{x}{a}\right)^3 - n_1^3\right]. \quad (8)$$

The total momentum carried away by the ejecta, which is of paramount importance for impact momentum transfer and asteroid deflection, can be found from integrating the mass  $dM$  ejected within a radial range  $dx$  for  $0 < x < R$ . Although this integration must be done numerically, Cheng et al. (2016) found that the cumulative ejecta momentum, normalised by the impactor momentum,  $\beta - 1$ , is well approximated by the analytical expression

$$\beta - 1 \approx \frac{9kC_1}{4\pi\sqrt{2}}\left(\frac{\rho}{\delta}\right)^{\frac{(\mu-\nu)}{\mu}}\frac{\mu}{3\mu-1}\left[\left(0.74n_2\frac{R}{a}\right)^{\frac{(3\mu-1)}{\mu}} - n_1^{\frac{(3\mu-1)}{\mu}}\right]. \quad (9)$$

One goal of the present work is to verify whether this expression is also a good approximation of ejected momentum in impact simulations. Note also that, as with the crater size scaling relationships (Eqs. (4) and (5)), the power-law exponents in the crater ejecta scaling relationships are functions of the same material-dependent velocity exponent  $\mu$ . An accurate characterisation of  $\mu$  for impacts on asteroid surfaces is therefore crucial for predictions of impact ejecta behaviour and momentum transfer.

### 3. Numerical model

To simulate vertical impacts on small asteroid surfaces, we used the iSALE2D shock physics code (Collins et al., 2004; Wünnemann et al., 2006), a multi-material, multi-rheology extension of the SALE hydrocode (Amsden et al., 1980). iSALE was specifically designed for simulating impact processes and is similar to the older SALEB hydrocode (Ivanov and Artemieva, 2002; Ivanov et al., 1997). It includes strength models suitable for impacts into geologic targets (Collins et al., 2004) and a porosity compaction model, the  $\epsilon - \alpha$  model (Wünnemann et al., 2006) that are both utilised here to mimic the material response of an asteroid surface.

While iSALE has been tested previously against laboratory-scale impacts (Luther et al., 2018; Wünnemann et al., 2016) and benchmarked against other hydrocodes (Pierazzo et al., 2008), here we compare iSALE predictions of ejection velocity vs. launch position against those recorded in experimental impacts in sand to build further confidence in simulation results. We therefore describe two suites of simulations: one replicating experimental impacts in sand and another exploring the influence of target properties on the outcome of impacts on small asteroids. The choice of input parameters for these two simulation suites are described in the relevant sections of the paper.

#### 3.1. Regridding and resolution tests

For an accurate description of the ejecta, the simulations must record the whole distribution of the ejecta. This is particularly problematic for the very high velocity particles ejected in the early phases of the simulations, which require high spatial resolution to capture accurately (Johnson et al., 2014). Also, due to the low strength of the target materials investigated, the craters grow many times larger than the projectile and over a long time-scale. To use a high resolution for the entire duration of the simulation can be highly computationally expensive. To overcome this, iSALE's regridding option was used. This option allows the computational grid to be coarsened by a factor of two after a predetermined amount of time. Three regrids were performed: the initial resolution was 40 cells per projectile radius (cpr) so that the final effective resolution was 5 cpr. Resolution tests (Fig. 1) showed that this method produces results (e.g., crater volume as a function of time) that are comparable to those obtained by a fixed, 40 cpr resolution but at an approximately equivalent cost to a fixed 5 cpr resolution run. At 10 ms, the fixed-resolution, 40 cpr run produces a crater volume of 19.43 m<sup>3</sup>, the fixed-resolution 5 cpr run, a crater volume of 18.41 m<sup>3</sup>, while the simulation with regridding produces a crater volume of 19.60 m<sup>3</sup>.

#### 3.2. Ejecta mass-velocity-launch position measurements

To track ejecta in the impact simulations, we used Lagrangian tracer particles that were placed across the high resolution domain. A simple and widely-used approach for identifying those tracers that comprise the crater ejecta is to flag the tracer as ejected during the simulation if its trajectory crosses a horizontal line a fixed altitude above the

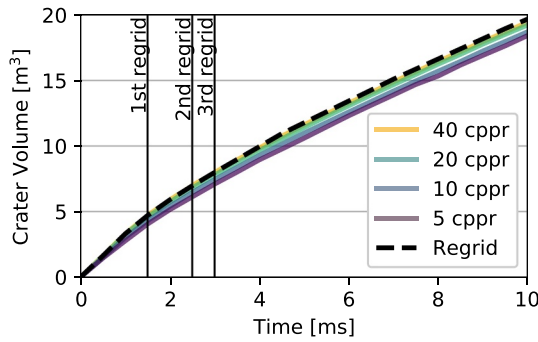


**Fig. 1.** Resolution test showing the crater volume growth against time, for a 0.84 m in diameter aluminium projectile, impacting a basalt target at 7 km/s simulation, with spatial resolutions between 5 and 40 cppr. Coarsening the domain by a factor of two at the times marked by the vertical lines (regrid) yields an accuracy comparable with the 40 cppr.

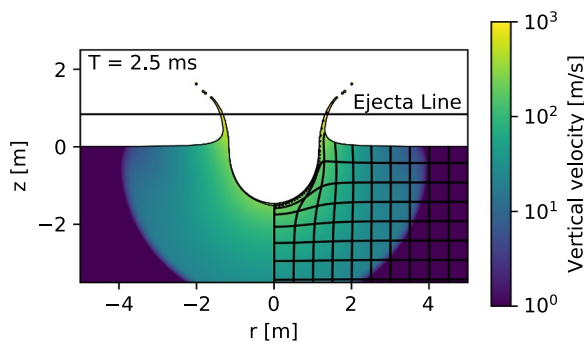


**Fig. 2.** Properties of the ejecta are recorded at the time the Lagrangian tracers cross the ejecta line, which was set at a height equal to one projectile diameter.

preimpact surface (Fig. 2). The mass, velocity vector, and launch position of each ejected tracer can then be recorded at the moment the tracer reaches this altitude. If this “ejecta line” happens to be placed at the height of the transient crater rim, the approach correctly distinguishes ejected material from that which remains in the crater or forms part of the uplifted rim. However, as the transient crater rim height is not known a priori, we adopted an ejecta line altitude equal to one impactor diameter.

To identify tracers that cross the ejecta line but should not be considered as part of the ejecta, because their final location was inside the crater or within the uplifted crater rim, the ejected tracers were also required to have a maximum speed exceeding that needed to overcome the cohesive strength of the target. In all cases simulated here we considered a velocity threshold of 10 cm/s, which was larger than the escape velocity of the asteroid, so that the momentum of the all ejecta contributed to momentum transfer.

To calculate the speed, angle and launch position of each ejecta tracer, we projected the tracer back from the location it crossed the ejecta line to the target surface. In zero- or very low-gravity scenarios it is sufficient to project back along a straight line trajectory, with a slope given by the ejecta velocity vector. However, in higher-gravity scenarios, such as those considered in the impact simulations replicating lab-scale experiments, it is important to project the ejected material back along a parabolic, ballistic trajectory. Defining the radius, horizontal and vertical velocity components of the ejecta at the surface and at the ejecta line as  $(x, u, v)$  and  $(x_h, u_h, v_h)$ , respectively, the assumption of a parabolic, constant gravity trajectory leads to:

$$u = u_h \quad (10)$$

$$v^2 = v_h^2 - 2gh \quad (11)$$

$$\alpha = \tan^{-1} \frac{v}{u} \quad (12)$$

$$x = x_h + \frac{u}{g} (v + \sqrt{v^2 + 2gh}). \quad (13)$$

where  $\alpha$  is the ejection angle (at the surface),  $h$  is the altitude of the ejecta line and  $g$  is the surface gravitational acceleration (negative down).

The surface-projected, ejected tracer data were processed to measure the mass/velocity/launch-position distributions of ejecta resulting from each impact cratering event as well as the cumulative ejected momentum as a function of ejection speed. We then used a numerical fitting procedure to determine the constants in various ejecta scaling relationships, Eqs. (7)–(9), and calculated the momentum enhancement factor,  $\beta$ .

#### 4. Model validation

Before investigating impacts into asteroid surfaces, iSALE's model accuracy was validated against data from laboratory impact experiments. Experiments aimed at studying the ejecta properties from impact cratering events have been performed by various research groups, summarised in Housen and Holsapple (2011). In this paper we focus on the data collected by Anderson et al. (2003), Cintala et al. (1999), Housen (2011, unpublished) and Hermalyn and Schultz (2011) (Table 1).

Cintala et al. (1999) conducted a series of laboratory experiments in which they impacted 4.76 mm aluminium spheres into coarse-grained (1–3 mm) sand targets, at velocities between 0.8 and 1.9 km/s. A laser-based system captured photographs of individual grains in their ballistic flight, that enabled them to fit parabolas through each ejecta trajectory and infer the ejection angle,  $\alpha$ , and ejection velocity,  $v$ , as a function of launch position,  $x$ .

In the Anderson et al. (2003) experiments, 6.35 mm aluminium spheres were impacted into finer-grained sand (0.5 mm), at velocities of about 1 km/s and various impact angles. The ejection angle,  $\alpha$ , and the ejection velocity,  $v$ , of the ejected particles were recorded using three-dimensional particle image velocimetry (3D PIV). This technique uses a system of lasers and digital cameras to illuminate a ring of particles, measuring the three-dimensional velocity vectors of the moving ejecta particles, at two slightly different positions. Numerical algorithms were then used to determine the instantaneous velocity vector from each pair of images. However, the digital camera only recorded one pair of images per impact experiment, so several shots of the same impact experiment were required to capture the ejecta curtain at different times in the crater growth evolution and to determine ejection velocity as a function of launch position.

Housen (unpublished work), which we refer to as Housen (2011, unpublished), performed quarter-space experiments of cylindrical polyethylene, magnesium and aluminium projectiles impacting dense sand targets, at speeds between 1.4 and 1.9 km/s. Results from these experiments were included in the synthesis of experimental impact ejecta studies by Housen and Holsapple (2011). The vertical impacts

**Table 1**  
Impact experiments summary.

Reference	Target			Impactor	
	Material	Grain size (mm)	Porosity (%)	Velocity (km/s)	Radius (mm)
Cintala et al. (1999)	Coarse sand	1–3	43	1.9	2.4
Anderson et al. (2003)	Loose sand	0.5	39	1.1	3.2
Housen (2011, unpublished)	Ottawa sand	1.0	32	1.4	6.1
Hermalyn and Schultz (2011)	Ottawa sand	1.0	35	5.6	3.2



were performed into a vacuum chamber. Coloured markers were placed into the target before the impact, and their trajectory was then measured by analysing footage of the impact recorded by a high-speed digital video camera (Housen and Holsapple, 2011).

Hermalyn and Schultz (2011) used a variety of projectiles to impact median grained Ottawa sand (1 mm) targets, at velocities of approximately 5 km/s. The experiment used a set of high-speed cameras and an imaging technique called Particle Tracing Velocimetry (PTV) to measure ejecta properties. Individual particles were tracked in their ballistic flight, in the plane of the ejecta curtain, which allowed the velocity of the ejecta particles to be derived as a function of time and launch position. The high frame rate allowed very fast ejecta to be recorded. However, the camera had a narrow field of view and did not record the slow ejecta near the final crater rim.

#### 4.1. Numerical model set-up

We simulated three impact experiments: the Cintala et al. (1999) experiment of a 4.76-mm diameter spherical projectile at 1.9 km/s (shot 4207 as defined in the Cintala et al., 1999 study), the Housen (2011, unpublished) impact of an 12.20-mm aluminium cylinder at 1.4 km/s and the Hermalyn and Schultz (2011) impact of an 6.35 mm aluminium spherical projectile at 5.6 km/s.

To simulate the sand targets, we used an ANEOS-derived equation-of-state (EOS) table for SiO<sub>2</sub> (Melosh, 2007) coupled with the  $\epsilon - \alpha$  porosity compaction model to describe the thermodynamic and volumetric response and the Drucker-Prager strength model to describe the shear response. This material model has been successfully used previously in validation work by Wünnemann et al. (2016). The Drucker-Prager strength model is a good description of the shear strength of granular materials, which defines the yield strength of the bulk material,  $Y$ , as  $Y = Y_0 + fP$ , where  $Y_0$  is the cohesion,  $P$  is the pressure,  $f$  is the coefficient of friction. In iSALE, the shear strength  $Y$  is capped at  $Y_m$ , which defines the limiting strength at high pressure. We note that the coefficient of internal friction,  $f$ , in the Drucker-Prager model is different from the coefficient of friction used in rock mechanics and in the Mohr-Coulomb model (Elbeshhausen et al., 2009), and can be approximately related to the angle of internal friction,  $\theta$ , as  $f \approx \sin(\theta)$ .

The angle of internal friction  $\theta$  was not measured for the coarse sand used in the experiments by Cintala et al. (1999), so we ran several test cases with  $f$  between 0.55 and 0.70. The best match of the ejecta distribution was achieved for  $f = 0.60$ . For the Housen (2011, unpublished) impact experiment we used  $f = \sin(35^\circ) \approx 0.55$  (Holsapple and Housen, 2012) and for the Hermalyn and Schultz (2011), we used  $f = \sin(30^\circ) = 0.50$  (Lee and Seed, 1967).

The target densities in the experiments were measured at 1.51 g/cm<sup>3</sup> (Cintala et al., 1999), 1.75 g/cm<sup>3</sup> (Housen, 2011, unpublished) and 1.70 g/cm<sup>3</sup> (Hermalyn and Schultz, 2011), which corresponds to porosities of  $\phi_0 = 0.42\%$ ,  $\phi_0 = 0.32\%$  and  $\phi_0 = 0.35\%$ , respectively. In the numerical simulations, these porosities were achieved by using the  $\epsilon - \alpha$  model (Wünnemann et al., 2006). The  $\epsilon - \alpha$  model takes in five input parameters, which are summarised in Table 2. The projectiles were modelled using the Tillotson (1962) EOS and the Johnson and Cook (1983) strength model for aluminium 1100-0, with  $A = 49$  MPa;  $B = 157$  MPa;  $C = 0.016$ ;  $m = 1.7$ ;  $n = 0.167$ ;  $T_{ref} = 800$  K (Benck et al., 1976; Pierazzo et al., 2008).

The iSALE simulations were run until the final crater was formed and all the ejected particles were recorded. As dry sand is cohesionless ( $Y_0 = 0$  Pa), the final crater diameter was much larger than the impactor diameter and the process occurred over a large simulation time, making the simulations computationally expensive. To reduce the time needed to run the simulations, the regridding option was used. The simulation had an initial resolution of 40 cpr and spatial resolution was coarsened three times by a factor of two, so that the latter stages of crater growth had an effective resolution of 5 cpr.

**Table 2**

Input target material model parameters used in the iSALE simulations.

Description	Symbol
Target	
Equation of state	ANEOS (quartzite) <sup>a</sup>
Strength model	Drucker-Prager
Poisson ratio	$\nu$ 0.30 <sup>b</sup>
Strength at zero pressure (MPa)	$Y_0$ 0
Strength at inf. pressure (MPa)	$Y_\infty$ 1000
Internal friction coefficient	$f$ 0.60/0.55/0.50
Porosity model parameters ( $\epsilon - \alpha$ ) <sup>b,c</sup>	
Initial porosity	$\phi_0$ 0.43/0.32/0.35
Initial distension	$\alpha_0$ 1.75/1.47/1.54
Elastic volumetric strain threshold	$\epsilon_{e0}$ -0.0013
Distension at transition to power-law	$\alpha_x$ 1.29 <sup>d</sup>
Exponential compaction rate	$\kappa$ 0.99 <sup>d</sup>
Ratio of porous/nonporous sound speed	$\chi$ 1.00

<sup>a</sup> Melosh (2007).

<sup>b</sup> Wünnemann et al. (2006).

<sup>c</sup> Collins et al. (2011).

<sup>d</sup> Wünnemann et al. (2016).

#### 4.2. Results and discussion

We first compared the results of the iSALE validation test with the Cintala et al. (1999) experiment. The ejection angle,  $\alpha$ , and the ejection speed,  $v$ , produced by the iSALE simulation are presented as a function of normalised launch position,  $x/R_r$ , in Fig. 3. We note that the crater radius used in the normalisation,  $R_r$ , was measured at the rim height in both the experiment and in the numerical simulation. Our numerical simulation produced a crater rim radius of about 11 cm, slightly larger than the experimental value of 9.1 cm. This difference may be attributed to combined effects of coarse resolution after the final regrid (5 cpr), as well as the coarse grains not being accurately represented by a continuous material model.

The angle of ejection was found to vary with launch position,  $x$ , in good agreement with the experimental results (Fig. 3a). The fast ejecta launched close to the impact site exhibits a steep ejection angle  $\approx 50^\circ$ ;  $\alpha$  then decreases with increasing launch position, until it reaches a minimum of  $\approx 35^\circ$ , after which  $\alpha$  increases again as the launch position approaches the final crater rim. A similar trend was observed by Cintala et al. (1999). The measured ejection speed,  $v$ , follows a power-law distribution, as predicted by the dimensional analysis of Housen et al. (1983) and the simulation results closely resemble the Cintala et al. (1999) experiment data.

Data from several studies similar to the Cintala et al. (1999) was then compared with the iSALE validation tests described above. Fig. 4 shows the normalised ejection speed as a function of normalised radial distance, as measured in the Anderson et al. (2003), Cintala et al. (1999), Housen (2011, unpublished) and Hermalyn and Schultz (2011) experiments. The ejection speed is normalised by the gravity scaling term  $\sqrt{gR}$  (Housen et al., 1983), and the launch position  $x$  is normalised by the crater radius,  $R$ , which this time is measured at pre-impact level.

The two experiments reproduced here, Housen (2011, unpublished) and Hermalyn and Schultz (2011) differ slightly in impact velocity and target properties from the Cintala et al. (1999) study. The two iSALE simulations are both in good agreement with the experimental data and as before, the ejection speed decreases with ejection distance following a power-law distribution. However the Hermalyn and Schultz (2010) data is shifted higher, probably due to the higher impact velocity, trend which is well replicated by our numerical simulations.

#### 5. Simulation set-up for DART scenario

Having proved iSALE's ability to simulate impact ejecta with a reasonable accuracy, we then simulated impacts into idealised asteroid surfaces and measured the mass/velocity/launch-position distributions

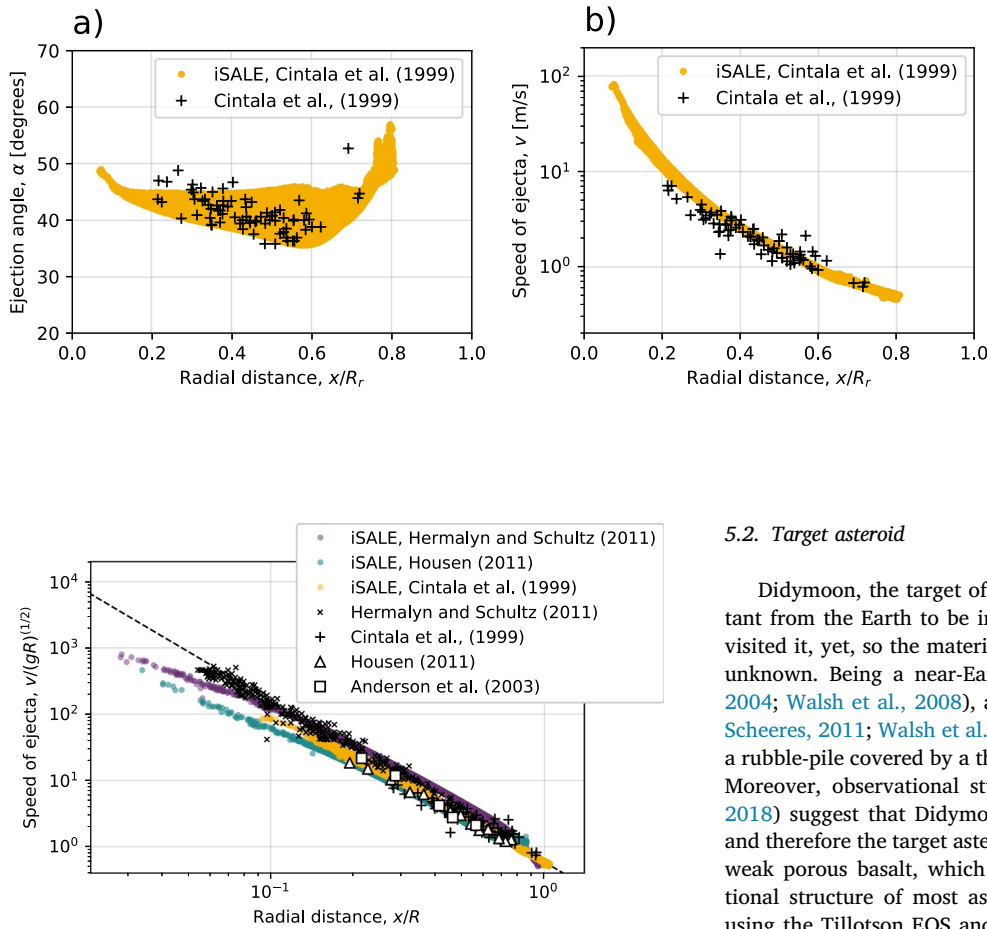


**Fig. 4.** Ejecta velocity distribution for iSALE impact simulations into sand targets, compared to the ejecta measurements from laboratory experiments, from Anderson et al. (2003), Cintala et al. (1999), Housen (2011, unpublished) and Hermalyn and Schultz (2011). For all data, the speed of the ejecta,  $v$ , is normalised by the gravity scaling term  $\sqrt{gR}$ , while the radial distance is normalised by the crater radius measured at the pre-impact level,  $R$ . The Cintala et al. (1999) crater radius data is converted from rim-height radius,  $R_r$ , to pre-impact level radius,  $R$ , using the relation  $R_r = 1.3R$ , as noted by Housen and Holsapple (2011). The Housen et al. (1983) power-law of  $\mu = 0.41$  (dashed line) is plotted for comparison.

of ejecta. To provide a practical reference point, the simulations were set up to resemble the DART scenario. The impactor was modelled as an aluminium sphere, while the target asteroid surface was modelled using a basaltic rock/regolith-like material model, with a fixed surface gravity of  $5 \times 10^{-5} \text{ m/s}^2$ .

### 5.1. Impactor

The impactor was modelled as a porous 0.84 m diameter sphere of mass 310 kg, using the Tillotson equation of state (EOS) and the Johnson-Cook strength model for aluminium (Johnson and Cook, 1983). The characteristics of the impactor were chosen to resemble a simplified spacecraft, with a bulk density of  $1000 \text{ kg/m}^3$ , accounting for the voids in the structure. The required porosity of 63% was represented using the  $\epsilon - \alpha$  porosity compaction model (Wünnemann et al., 2006). The  $\epsilon - \alpha$  model parameters are not known for aluminium, so used the nominal parameters:  $\alpha_0 = 2.7$ ,  $\alpha_x = 1.0$ ,  $\kappa = 0.9$ ,  $\chi = 1.0$ . The impactor properties and impact velocity (7 km/s) were kept constant for all simulations in the following sections.

**Fig. 3.** Ejecta distribution produced by iSALE, represented by yellow points, compared to the ejecta distribution measured from shot 4207, in the Cintala et al. (1999) experimental study (black crosses). The iSALE simulation used a 2.4 mm aluminium sphere, at 1.9 km/s, impacting a half-space quartzite target, with 43% porosity and a coefficient of friction of  $f = 0.6$ . a) Ejection angle, in degrees, as a function of radial distance,  $x$  normalised by the crater radius,  $R_r$ . b) Speed of the ejecta, in m/s, as a function of normalised radial distance. The crater radius,  $R_r$ , was measured at rim height in both the simulation and in the experiment. (For interpretation of the references to colour in this figure legend, the reader is referred to the web version of this article.)

### 5.2. Target asteroid

Didymoon, the target of the DART spacecraft, is too small and distant from the Earth to be individually resolved and no spacecraft has visited it, yet, so the material properties and the internal structure are unknown. Being a near-Earth double system asteroid (Durda et al., 2004; Walsh et al., 2008), affected by the YORP effect (Jacobson and Scheeres, 2011; Walsh et al., 2012), it is most likely that the asteroid is a rubble-pile covered by a thin layer of regolith (Murdoch et al., 2017). Moreover, observational studies (Michel et al., 2016; Michel et al., 2018) suggest that Didymos is an S-type siliceous asteroid system, and therefore the target asteroid material was considered to be made of weak porous basalt, which is a good approximation of the compositional structure of most asteroids. The basaltic target was modelled using the Tillotson EOS and one of two different strength models, referred to in this paper as LUND and ROCK.

### 5.3. The LUND and ROCK strength models

Didymoon is approximately 160 m in diameter (Michel et al., 2016), with extremely low surface gravity, which means that the impact crater will most likely form in the so-called strength regime. This is because at such low gravity the resistance to crater growth from the weight of the displaced target is small, while the resistance from the strength of the target material is very important even if the material is weak. Therefore, the accuracy of the strength model used to describe the response of the asteroid surface is paramount. The strength model describes the limiting shear stress that the material can support, which can be a function of pressure, temperature and strain.

The LUND model in iSALE is a simple pressure-dependent strength model typical of geologic materials (Lundborg, 1967), which asymptotes to a certain strength at high pressure and is not dependent on strain or damage. The Lundborg strength model defines the yield strength as (Collins et al., 2004)

$$Y = Y_{d0} + \frac{fP}{1 + \frac{fP}{Y_{dm} - Y_{d0}}}, \quad (14)$$

where  $P$  is pressure,  $f$  is the coefficient of internal friction and  $Y_{dm}$  is the limiting strength for damaged material, at high pressure.

The ROCK model in iSALE is a more complex model, in which strength is reduced as strain accumulates. The ROCK strength model defines the yield strength as (Collins et al., 2004)

$$Y = Y_d D + Y_i (1 - D), \quad (15)$$

where  $D$  is a scalar measure of damage, which is itself a function of accumulated plastic strain. The damaged material strength,  $Y_d$ , is defined by a Drucker-Prager relationship:

$$Y_d = \min(Y_{d0} + fp, Y_{dm}). \quad (16)$$

The intact material strength,  $Y_i$ , is defined by the Lundborg relationship:

$$Y_i = Y_{i0} + \frac{f_i p}{1 + \frac{f_i p}{Y_{im} - Y_{i0}}}, \quad (17)$$

where  $f_i$  is the coefficient of internal friction for intact material,  $Y_{im}$  is the limiting strength at high pressure for intact material,  $f$  is the coefficient of internal friction for damaged material and  $Y_{dm}$  is the limiting strength for damaged material at high pressure. In this work, we used the damage model described by Ivanov et al. (2010) to relate plastic strain to  $D$ .

For the DART-scale simulations, when the ROCK model was used, the strength of the intact material was varied between 10 and  $10^3$  kPa, while the strength of the damaged material was varied between 0.1 and 10 kPa. Preliminary tests designed to compare the simulation results between the LUND model with  $Y_{d0} = 1$  kPa and ROCK model with  $Y_{d0} = 1$  kPa and  $Y_{i0} = 10$ , 100 and 1000 kPa, showed that the two strength models produce simulations that exhibit minimal differences for our specific material parameters. In terms of crater dimensions, the LUND strength model produced craters with volumes  $\approx 13\%$  smaller than the ROCK model, while the crater radius produced was almost the same in all cases. Furthermore, all models produce very similar ejecta distributions. This suggests that it is the post-shock (damaged) strength of asteroid surface, rather than the intact (or pre-impact) strength, that controls impact ejecta behaviour. Hence, the LUND strength model describing a (pre)damaged target was preferred for simplicity and computational expedience.

We note that the range for the cohesive strength of the target material  $10 < Y_{d0} < 1000$  kPa chosen in this work is lower than in previous asteroid deflection studies. For example, Jutzi and Michel (2014) used a cohesion of 100 MPa, Stickle et al. (2015) used  $\approx 200$ –300 kPa, while Syal et al. (2016) investigated cohesions between 1 kPa and 3.5 GPa. Our choice of cohesion for the damaged target material was based on estimates of the cohesion of the lunar regolith (Heiken, 1991; Holsapple and Housen, 2012), which we expect to be a good analog of both asteroidal regolith as well as rocky asteroidal material after it has been fractured by an impact-generated shock wave.

#### 5.4. Internal friction

The coefficient of internal friction,  $f$ , cannot be measured remotely and, in asteroids, can take a range of values. Our numerical simulations used coefficients  $f$  between 0.2 and 1.2. However, values lower than 0.5 and higher than 1.0 are very unlikely, based on geological analogs, while the most common value for geological materials is around 0.6 (Goodman, 1989).

#### 5.5. Porosity

The asteroids in the Solar System have been observed to have a large range of porosities,  $\phi_0$ , even up to 50% porosity in the case of asteroid 253 Mathilde (Yeomans et al., 1997). In our simulations, the porosity of the asteroid was modelled using the  $\epsilon - \alpha$  model (Wünnemann et al., 2006) and its value was varied between 10% and 50%. The simulation parameters are summarised in Table 3.

### 6. Results for DART scenario

We can divide our numerical simulations into three distinct systematic parameter studies, aimed at investigating the isolated effects of cohesion (shear strength at zero pressure),  $Y_{d0}$ , initial porosity,  $\phi_0$ , and the internal friction coefficient,  $f$ . Final crater dimensions, mass/velocity/launch-position distributions of the ejecta and, subsequently, the momentum carried away by the ejecta,  $\beta - 1$ , were calculated using

**Table 3**

Material model parameters for simulations of the DART impact. In addition, thermal parameters from Ivanov et al. (2010) were used.

Description	Symbol	Target
Equation of state		Tillotson <sup>a</sup>
Strength model		ROCK/LUND
Poisson ratio	$\nu$	0.25 <sup>b</sup>
Damage strength at zero pressure (kPa)	$Y_{d0}$	0.1–100
Strength at infinite pressure (MPa)	$Y_{inf}$	$10^3$
Internal friction coefficient	$f$	0.2–1.2
Porosity model parameters ( $\epsilon - \alpha$ ) <sup>c</sup>		
Initial porosity	$\phi_0$	10–50%
Initial distension	$\alpha_0$	1.1–2.0
Elastic volumetric strain threshold	$\epsilon_{e0}$	$-2 \times 10^{-6}$ to $-2 \times 10^{-9}$
Distension at transition to power-law	$\alpha_x$	1.00
Exponential compaction rate	$\kappa$	0.80–0.98
Ratio of porous/nonporous sound speed	$\chi$	1.00

<sup>a</sup> Tillotson (1962).

<sup>b</sup> Ivanov et al. (2010).

<sup>c</sup> Wünnemann et al. (2006).

results from simulations with different combinations of these numerical parameters.

#### 6.1. The effect of target properties on crater diameter

As discussed before, the crater size is strongly linked with the amount of ejecta produced, and hence with the amount of momentum transferred. Furthermore, the scaled crater diameters provide a method for determining the scaling exponent,  $\mu$ .

In this section, we investigate the effects of target properties on crater dimensions, and compare the widely-used strength-regime crater scaling relationship Eq. (4), to our simulation results. For all of our models, the derived scaling exponent,  $\mu$ , ranges between the momentum scaling limit,  $\mu = 1/3$ , and the energy scaling limit,  $\mu = 2/3$ .

The strength-scaled crater diameters for target porosities  $\phi_0 = 10\%$ , 20% and 50%, and an internal friction coefficient  $f = 0.6$ , are plotted in Fig. 5. These results have been plotted alongside experimental results from materials which seem to be appropriate analogs for porous rocky asteroid surfaces: weakly cemented basalt (WCB) (Housen, 1992), and sand/fly ash (SFA) (Housen and Holsapple, 2003).

The numerical simulation results lie between the scaling law extrapolations of experimental data, and follow a power-law trend with a slope between  $\mu = 0.40$  and  $\mu = 0.43$ , which is similar to the slope of the expected trend for WCB ( $\mu = 0.40$ ) and SFA ( $\mu = 0.46$ ). These results suggest that the crater diameters predicted by the numerical simulations are consistent with the existing scaling laws for analogous materials, from lab-scale impact experiments, when the lower cohesion of the targets are taken into account. The target material strength used in the numerical simulations was closer to the estimate of the asteroid's regolith strength (Heiken, 1991).

To isolate the effect of target cohesion, we then consider the simulation results with different  $Y_{d0}$ , between 0.1 and 100 kPa, but with a fixed initial target porosity of 20% and a coefficient of internal friction of 0.6. As all simulated impact craters form in the strength regime, the crater dimensions are very sensitive to  $Y_{d0}$ . Crater excavation becomes more efficient as the target material strength exhibits less resistance to the crater growth. The crater diameters were found to vary from about 36 m at 0.1 kPa to about 9 m at 100 kPa. By least-square fitting the point-source scaling law in the strength regime, Eq. (4), to the scaled crater diameter,  $D(\rho/m)^{(1/3)}$ , as a function of strength-scaled impact size,  $Y_{d0}/(\rho U^2)$ , we derived the velocity exponent,  $\mu$ . For this scenario,  $\mu$  holds a value of  $0.42 \pm 0.01$ .

To measure the additional effect of porosity on the crater dimensions, we consider the results of four series of simulations with initial target porosity between  $\phi_0 = 10\%$  and  $\phi_0 = 50\%$ , and with a fixed

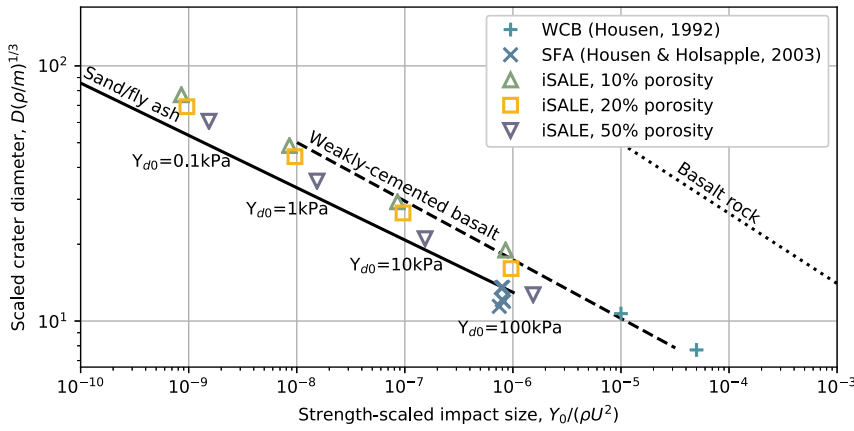


**Fig. 5.** Scaled crater diameter as a function of strength-scaled impact size for iSALE simulations at 10%, 20% and 50% porosity, compared with the extrapolations of the experimental results for weakly-cemented basalt (WCB) (Housen, 1992) and sand/fly ash (SFA) (Housen and Holsapple, 2003). Note that the scaled crater diameter is the diameter of the formed crater,  $D$ , multiplied by the square cube of the target density,  $\rho$ , and divided by the impactor mass,  $m$ , is plotted against the strength-scaled impact size (the surface strength,  $Y_0$ ) divided by the target density,  $\rho$ , and the square of the impactor velocity,  $U$ .

coefficient of internal friction constant of  $f = 0.6$ . For each target porosity, the series of simulations included four different target cohesions,  $Y_{d0} = 0.1, 1, 10$  and  $100$  kPa.

Consistent with previous work (e.g., Luther et al., 2018), as the porosity of the target material is increased the cratering efficiency decreases slightly. The presence of porosity leads to more energy being used in pore compaction, which leaves less energy available to displace material. On the other hand, with increasing porosity the material becomes less dense and easier to excavate. Our results suggest that the former effect dominates slightly over the latter as an increase in target porosity from 10% to 50% leads to a decrease in crater diameter and crater volume of only 20%, while the crater depth remains almost the same.

Least-square fits of Eq. (4) through resulting crater dimensions at different porosities and different cohesive strengths, as illustrated in Fig. 6a, determined the scaling exponent,  $\mu$ , for each set of simulations. The  $\mu$  parameter was found to slightly increase with target porosity, from  $\mu = 0.40$  at 10% porosity to  $\mu = 0.43$  at 50% porosity. This is contrary to expectation from some laboratory scale cratering experiments, but is consistent with recent numerical simulations of simple crater formation on the Moon (Priour et al., 2017).

To quantify the effect of the internal friction coefficient on crater dimensions, we consider the results of six series of simulations with different coefficients of friction,  $f$ , between 0.2 and 1.2, and with a fixed initial porosity  $\phi_0 = 20\%$ . Each simulations series included the same set of target cohesions  $Y_{d0} = 1, 10$  and  $100$  kPa. An increase in  $f$  has the effect of significantly reducing the cratering efficiency. A larger coefficient of internal friction in the target material causes more energy to be used in deforming the target and leaves less to excavate the material out of the crater. The crater radius when  $f = 0.2$  is more than twice the crater radius formed for  $f = 1.2$  (Fig. 6b).

The  $\mu$  exponent was found to decrease with increasing internal

friction coefficient, from approximately  $\mu = 0.48$  at  $f = 0.2$ , to approximately  $\mu = 0.35$  at  $f = 1.2$ , which is close to the lower (momentum) theoretical limit for  $\mu$ .

## 6.2. The effect of target properties on ejecta distribution

In addition to crater diameters, we also quantified ejecta mass/velocity/launch-position distributions for each simulation. In this section we describe the effect of cohesion, porosity and internal friction coefficient on the ejecta distributions.

### 6.2.1. Cohesion

Fig. 7a shows the cumulative normalised ejecta mass at speeds larger than  $v$ ,  $M(>v)/m$ , as a function of normalised ejection velocity,  $v/U$ , for four impacts simulations into targets with  $\phi_0 = 20\%$ ,  $f = 0.6$  and  $Y_{d0}$  between 0.1 kPa and 100 kPa. Our results show that the fast ejecta ( $v/U > 10^{-2}$ ) follow the same mass-velocity distribution, regardless of the cohesion; the effects of varying  $Y_{d0}$  being negligible. However, towards the end of crater growth when material is ejected at slower speeds,  $Y_{d0}$  becomes increasingly important. In the strength regime, the cohesion is the dominant stress that stops the crater from growing and as  $Y_{d0}$  is decreased, crater growth continues longer, leading to a greater total ejected mass and more material ejected at a given velocity in the latter portion of crater growth.

Ejecta measurements of normalised ejecta speed,  $v/U$ , as a function of normalised launch position,  $x/a$ , from the same simulations are plotted in Fig. 7b. Again, the fast ejecta from the four simulations, launched at similar distances from the impact point,  $x/a$ , have the same speed, following the same power-law distribution. An increase in the target cohesion stops the crater from growing, and the launch of ejecta, at a smaller radius. The relatively large scatter in radial distance (launch position) among the slowest ejecta is because this is material

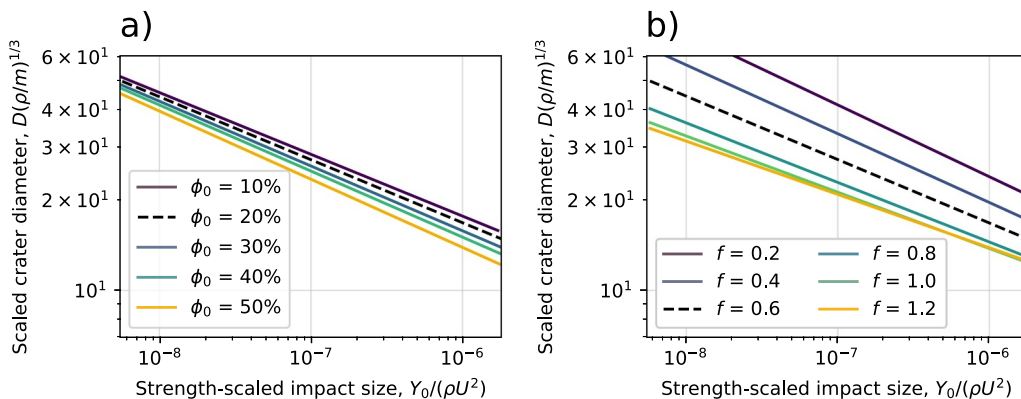


**Fig. 6.** Least-square power-law fitting through normalised crater diameter,  $\pi_D$  as a function of strength-scaled impact size,  $\pi_3$ , in logarithmic scale, for asteroid targets with a) different initial porosities,  $\phi_0$  ( $f = 0.6$  for all simulations) and b) different internal friction coefficients,  $f$  ( $\phi_0 = 20\%$  for all simulations). In both plots, the dashed line represents the results for  $\phi_0 = 20\%$  and  $f = 0.6$ .



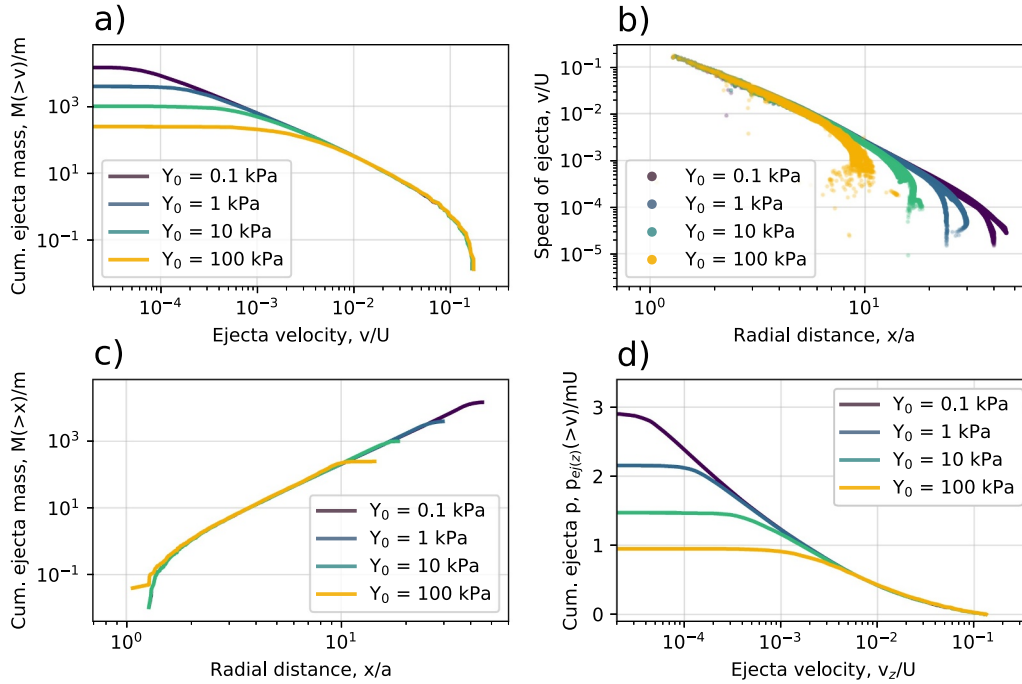


Fig. 7. Mass-velocity-launch position distribution of ejecta for four different strengths: 0.1, 1, 10 and 100 kPa, for a target with  $\phi_0 = 20\%$  and  $f = 0.6$ .

ejected from the uplifted rim region with sufficient speed to overcome the cohesive strength of the target.

Fig. 7c shows the normalised mass of ejecta launched within a radius  $x$ ,  $M(<x)/m$ , as a function of normalised launch position,  $x/a$ . In this case, the ejecta distributions from the four simulations are very similar. While the cohesion does not influence the amount of ejected mass at a given launch position, it does dictate the maximum radial distance at which particles are ejected, for a given crater.

The ejecta mass-velocity distributions were integrated to determine the cumulative, vertically ejected momentum,  $p_{ej(z)}/mU = (\beta - 1)$ , as a function of ejection speed in the vertical direction  $v_z$  (Fig. 7d). Most of the ejecta momentum resides in the slowest ejecta, which is last to leave the crater. The total ejected momentum depends strongly on the total ejected mass (and crater size) and, hence,  $Y_{d0}$ . This leads to  $\beta - 1$  values between  $\approx 1.0$  and  $\approx 3.0$ .

### 6.2.2. Porosity

An increase in target porosity causes the tracer particles close to the impact point to be ejected at lower speeds compared to the less porous cases, as illustrated in Fig. 8a. For porous targets, more of the energy imparted from the impactor is used to compact the pores, making less available to set the target material in motion and eject material. In addition, as the target is made more porous, the ejected material becomes less dense and so less total mass is ejected from the same radial distance, compared to the denser lower porosity targets. As a consequence, the total momentum transferred by the ejecta, normalised by the impactor momentum,  $\beta - 1$  decreases with increasing porosity, as shown in Fig. 8b.  $\beta - 1$  was found to vary between 1.1 at  $\phi_0 = 50\%$  and 2.7 at  $\phi_0 = 10\%$ .

### 6.2.3. Internal friction coefficient

Near the impact site, the friction coefficient has little or no influence on the ejecta distribution. The normalised ejected mass  $M(>v)/m$ , plotted against the normalised ejection speed,  $v/U$ , in Fig. 8c, shows that the effects of coefficient of friction are only visible for  $v/U < 5 \times 10^{-2}$ . With increasing  $f$ , more energy is needed to deform the target and this has the effect of slowing down the ejection speed of the tracers ejected at the same radial distance.

In terms of total momentum transfer, because increasing the coefficient of friction has the effect of slowing down the ejecta, less momentum is carried away by the ejected particles. The difference between  $\beta - 1$  at high  $f$  (0.6 to 1.2) is very large compared with the cumulative ejecta momentum at low  $f$  (0.2 to 0.4) as seen in Fig. 8d.

The behaviour of the ejecta in our numerical simulations is consistent with impact experiments. Housen and Holsapple (2011) compared the ejection velocity from impacts into dry sands ( $\phi_0 \approx 30\text{--}40\%$ ), with ejection velocities from impacts into porous silicates and sand mixtures ( $\phi_0 \approx 55\text{--}83\%$ ), and noted that the highly porous materials had much lower ejecta velocity compared to the less porous sands. Luther et al. (2018) also observed a similar trend in their numerical impact simulations in the gravity regime.

When comparing the ejection velocity from impact experiments into materials of different internal friction coefficients, no clear trend was determined (Housen and Holsapple, 2011). They note that impact experiments into glass micro-spheres ( $f \approx 0.35$ ) (Yamamoto et al., 2005) produced a much higher ejection velocity compared to impacts into sand ( $f \approx 0.50\text{--}0.60$ ). However, the results were not reproduced by Housen (2011, unpublished) so Housen and Holsapple (2011) concluded that the higher velocity might be produced by other material properties. Our observed trend for the ejection velocity is again consistent with numerical impact simulations in the gravity regime (Luther et al., 2018).

## 7. Discussion

### 7.1. Implications for the DART mission

Our simulations deliberately considered impactor and target parameters appropriate for the DART mission and the Didymos asteroid system, allowing us to directly relate our numerical results to the DART impact and infer possible deflection outcomes.

In all of our numerical simulations, the asteroid deflection was amplified by the impact ejecta, i.e.  $\beta - 1 > 0$ . However, the amount by which the deflection was amplified depended strongly on the target properties. Fig. 9 shows the momentum carried away by the ejecta,  $\beta - 1$ , for different impact scenarios, as a function of target porosity

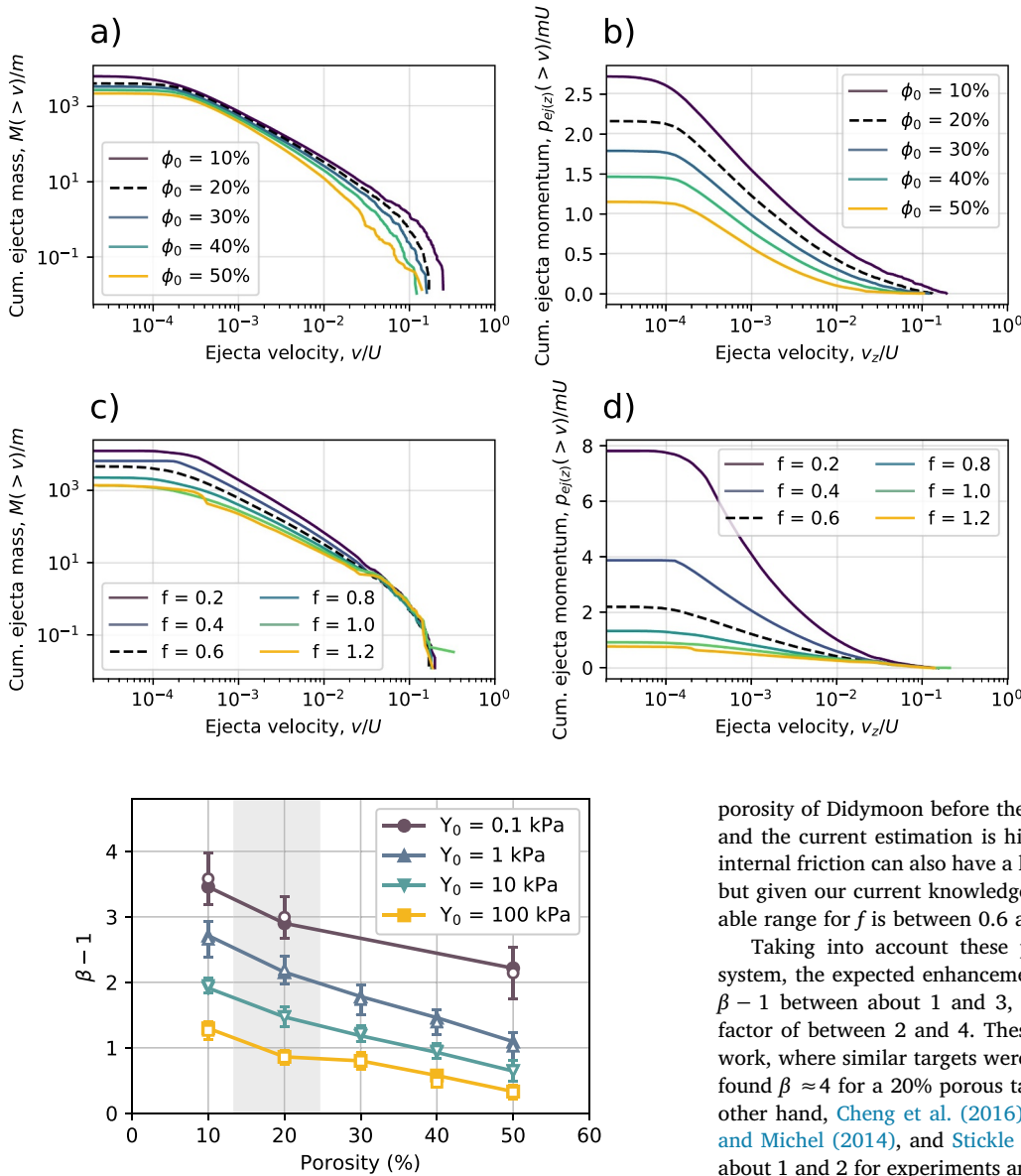


**Fig. 9.** Total ejected momentum in the  $z$  direction ( $\beta - 1$ ) for four different cohesions and different porosities of the target. The numerical value of the ejected momentum (filled symbols) is compared with the analytical approximation of  $\beta - 1$  (hollow symbols). The grey shaded region is the current estimate of the  $\phi_0$  of Didymoon (Scheirich and Pravec, 2009).

and at different target strengths. We found that  $\beta - 1$  can vary between 0.5 and 3.5.

We investigated impacts into porous targets at  $Y_{d0}$  between 0.1 and 100 kPa, and found that the amount of momentum transferred from the impactor is mainly driven by the cohesive strength of the target. The weaker the target, the more deflection we should expect. Unfortunately, for DART, we will not be able to measure the cohesive strength of the target before the impact or to select the impact site. DART could hit anything from a smooth, very weak terrain, with  $Y_{d0}$  even lower than our investigated range, which would provide a very large deflection of the asteroid, or it could hit a strong boulder, which could result in almost no momentum enhancement.

The porosity of the surface material can also influence the deflection, but not as considerably as the cohesive strength. An increase in porosity of 10% can decrease  $\beta - 1$  by up to 0.5, for a given target material. However, assuming the primary and secondary objects of the Didymos system have the same density, we can approximate the

**Fig. 8.** Normalised ejected mass at speeds greater than  $v$ , as a function of normalised ejection speed,  $v/U$ , and total ejected momentum ( $\beta - 1$ ) as a function of normalised ejection velocity. a) and b) represent the ejecta distributions for impacts into targets with  $Y_{d0} = 10$  kPa,  $f = 0.6$  and  $\phi_0$ , between 10% and 50%. c) and d) represent ejecta distributions for impacts into targets with  $Y_{d0} = 10$  kPa,  $\phi_0 = 20\%$  and  $f$ , between 0.2 and 1.2.

porosity of Didymoon before the impact (Scheirich and Pravec, 2009), and the current estimation is highlighted in Fig. 9. The coefficient of internal friction can also have a large effect on the momentum transfer, but given our current knowledge of asteroid materials, the most probable range for  $f$  is between 0.6 and 0.8.

Taking into account these predictions for the Didymos asteroid system, the expected enhancement resulting from the DART impact is  $\beta - 1$  between about 1 and 3, implying a momentum multiplication factor of between 2 and 4. These values are consistent with previous work, where similar targets were used. For example, Syal et al. (2016) found  $\beta \approx 4$  for a 20% porous target with a cohesion of 1 kPa. On the other hand, Cheng et al. (2016), Holsapple and Housen (2012), Jutzi and Michel (2014), and Stickle et al. (2015), found  $\beta$  values between about 1 and 2 for experiments and simulations in which much stronger targets (cohesions of a few MPa) were used. These results reinforce our conclusion that for impacts on small asteroid surfaces  $\beta$  is most sensitive to the cohesion of the target.

The numerical simulations presented here provide insight to inform future impact deflection missions. However, an important limitation of our numerical simulations is the use of a two-dimensional domain geometry, which restricted our study to vertical impacts, with cylindrically-symmetric ejecta distributions. In such scenarios, the net ejecta momentum is antiparallel to the impact direction, resulting in maximum efficiency of momentum enhancement by ejecta. In reality, the DART spacecraft will likely impact Didymoon's surface at an oblique angle (Cheng et al., 2018), which will produce an asymmetric distribution of ejecta with a net momentum vector that points in a different direction to the impact trajectory. Simplified, 2D impact simulations were used here for computational expediency to allow for a wide range of target properties to be investigated. Further work to simulate oblique impacts in three dimensions is clearly needed to develop ejecta scaling relationships for oblique impacts and quantify the role of the impact angle in impact momentum transfer. Full three-dimensional impact simulations will also identify whether any other consequences of a simplified cylindrical geometry, such as restrictions in the geometry of damage propagation, play a significant role in momentum transfer.

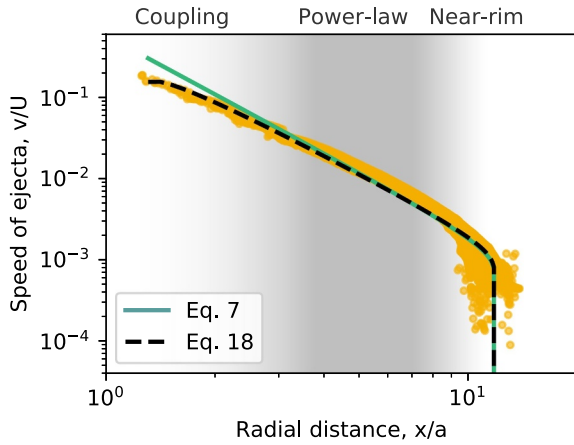


**Fig. 10.** Normalised ejection speed,  $v/U$ , as a function of normalised launch position,  $x/R$  for an impact into a target with 1 kPa cohesion and 20% porosity. The ejecta distribution has three distinct regions: coupling zone, power-law region and near-rim region, denoted by the background shading.

### 7.2. Ejecta scaling relations

Our simulation results also prompt a closer inspection of the ejecta mass-velocity-launch position distributions and comparison with the recently refined ejecta scaling relationships of Housen and Holsapple (2011). In particular, an ongoing controversy is whether impact crater dimensions and ejecta distributions from impacts in the same material produce consistent values of the velocity exponent  $\mu$  and what, if anything, this means for the suitability of the point-source approximation. We also seek to verify the analytical estimation of the ejecta momentum transfer,  $\beta - 1$ , presented by Cheng et al. (2016).

Examining the velocity distribution of ejecta as a function of launch position, three regimes of ejection velocity behaviour are apparent (Housen and Holsapple, 2011), as illustrated in Fig. 10. The mid-ranged ejecta follows a power-law distribution, which is well described by the Housen et al. (1983) ejecta model. This power-law behaviour breaks down close to the crater rim, where the ejection velocity rapidly decreases. An empirical correction to account for this behaviour was introduced by Housen and Holsapple (2011) in their revised ejecta model. However, close to the impact point there is the coupling zone, where the projectile is still transferring its energy and momentum to the target. In our simulations, the ejection velocity in this zone is slower than the extrapolated power-law distribution identified for the mid-range ejecta and neither analytical model accounts for this behaviour. The transition between the regimes is gradual and the radial range of each stage is dependent on the projectile and target properties (Hermalyn and Schultz, 2010). For impacts with low cratering

efficiency, the coupling stage becomes more important and covers a larger portion of the crater growth time (Schultz, 1988; Schultz, 1992), transitioning directly into the near-rim regime and causing the power-law regime to be almost or entirely non-existent.

In most previous studies of ejection velocity behaviour, both experimental and numerical data were interpreted in the context of the Housen et al. (1983) or Housen and Holsapple (2011) ejecta models. However, in several cases this has resulted in  $\mu$ -values being determined from ejecta data that are inconsistent with the  $\mu$ -value determined from crater size measurements for the same target material (Cintala et al., 1999; Luther et al., 2018; Tsujido et al., 2015; Yamamoto et al., 2017). This has raised doubts about the applicability of the ejecta scaling relationships and questions regarding how to best determine  $\mu$  for a particular target material. Here we investigate the circumstances under which consistency can be achieved between  $\mu$  values determined from both crater scaling and ejecta scaling.

To study this problem further, we compared values of the velocity exponent,  $\mu$ , determined by fitting the Housen et al. (1983) power-law (Eq. (6)) to ejecta data; by fitting the Housen and Holsapple (2011) ejecta scaling relationship (Eq. (7)) to ejecta data; and by fitting the strength-regime crater scaling relationship (Eq. (4)) to crater size data. According to the point-source theory, the scaling exponent  $\mu$  determined from ejecta should be consistent with that determined from the crater scaling.

To fit the Housen et al. (1983) ejecta scaling relationship, Eq. (6), to our ejecta data we used a least-squares fitting algorithm applied only to the power-law regime of velocity-launch position distribution; in other words, the fast and the slow ejecta in the coupling zone, and near-rim zone, respectively, were excluded from the analysis. However, due to the gradual transition between the ejection zones, it is difficult to choose the appropriate limits on the launch distance  $x$  for fitting. To account for the coupling zone (fast ejecta), we excluded the ejecta with a radial distance  $x < 4a$ , where  $a$  is the impactor radius. To exclude the slow ejecta, we only considered the ejected particles from within  $x < 0.74R$ , where  $R$  is the crater radius. These choices of threshold radii were chosen based on the range of ejecta behaviour observed in our simulations and have proven to give good results, as discussed below. We note, however, that together they place a lower limit of  $\approx 6$  on the cratering efficiency of impacts that can be used to derive a power-law ejecta trend, because of the requirement that  $4a < 0.74R$ . The fitting algorithm was set to return values for the scaling exponent  $\mu$  and the constant  $C_1$ , while the other constants were fixed:  $n_1 = 1.2$ ,  $n_2 = 1$  and  $\nu = 0.4$  (Housen and Holsapple, 2011).

When fitting Eq. (7) to our ejecta data, we considered the entire range of the ejecta velocity-launch position distribution. In this case, the fitting algorithm set  $C_1$  and  $\mu$  as free parameters, while the other constants were fixed. The  $p$  constant was also fixed, at  $p = 0.2$ , in order to reduce errors in the fitting algorithm. Previous studies used larger  $p$

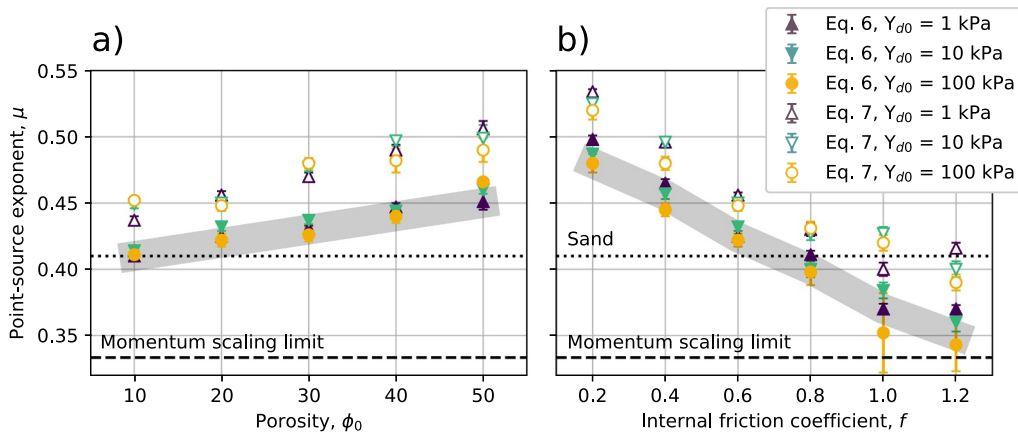


**Fig. 11.** Ejecta velocity-launch position distribution fitting results. Filled markers represent the results from fitting Eq. (6) (Housen et al., 1983), hollow markers denote results from fitting Eq. (7). a) the scaling exponent  $\mu$  is presented as a function of porosity, for fixed coefficient of internal friction,  $f = 0.6$ ; b) the scaling exponent  $\mu$  is presented as a function of internal friction coefficient, for fixed porosity,  $\phi_0 = 20\%$ . The shaded area represents the crater scaling results.

values, 0.5 for basalt rock, 0.3 for WCB and 0.2 only for perlite/sand mixture (Housen and Holsapple, 2011).

Fig. 11 shows the scaling exponent  $\mu$  returned by the fitting algorithm for ejecta data from each simulation, as a function of cohesion,  $Y_{d0}$ , porosity,  $\phi_0$ , and coefficient of internal friction,  $f$ . The scaling exponent,  $\mu$ , obtained from the power-law (Eq. (6)) fitting is represented by filled markers, while the  $\mu$  obtained from fitting Eq. (7) is represented by hollow markers. The two sets of scaling exponents are compared to the  $\mu$ -value determined from crater scaling (see Section 6.1), which are represented by the shaded grey region. Our results show that the scaling exponent  $\mu$  determined using a simple power-law (for  $4a < x < 0.74R$ ) is in good agreement with the  $\mu$ -value obtained from crater size scaling, while using Eq. (7) produces  $\mu$ -values that are systematically larger.

### 7.3. A revised ejecta scaling relationship

To avoid the need for somewhat arbitrary exclusion of some ejecta data to determine the velocity exponent  $\mu$  by a simple power-law fit, we also considered a modified version of the (Housen and Holsapple, 2011) ejection model (Eq. (7)) that attempts to account for the coupling zone of the ejecta distribution. Our revised expression includes an additional term dependent on the  $n_1$  cut-off constant, the impactor radius,  $a$ , and a new fitting constant,  $q$

$$\frac{v(x)}{U} = C_1 \left[ \frac{x}{a} \left( \frac{\rho}{\delta} \right)^{\frac{1}{q}} \right]^{-\frac{1}{\mu}} \left( 1 - \frac{x}{n_2 R} \right)^p \left( 1 - \frac{n_1 a}{x} \right)^q. \quad (18)$$

Preliminary studies showed that  $q$  holds a value between 0.1 and 0.2. It is also important to note that this equation only holds for  $x > n_1 a$  and  $x \leq n_2 R$ .

To test this new approach, we used a least-squares method to fit Eq. (18) to the simulation model data, and determine the scaling exponent  $\mu$ . Fig. 10 shows the best fits of Eq. (7) and of Eq. (18) (dashed line), to the velocity-launch position distribution of the ejecta from an impact simulation with  $Y_{d0} = 10$  kPa,  $f = 0.6$ , and an initial porosity of 20%. Eq. (18) was fitted to the entire range of the data, while Eq. (7) was only fitted through the power-law and the near-rim regions. Even though the two equations appear quite similar graphically, they return different values for the fitting constants. Fig. 12 shows the velocity exponent  $\mu$  as a function of porosity and internal friction coefficient, obtained by fitting Eq. (18) to the ejecta data. In almost all cases, fitting Eq. (18) to our model data results in  $\mu$ -values that are consistent between ejecta scaling and crater scaling, and this is achieved without any exclusion of ejecta data or choice regarding the radial range over which power-law behaviour is present.

### 7.4. Practical application of ejecta scaling

Further validation work of Eq. (18) is required to determine the limits of its applicability. Firstly, it is important to note that the equation can only be used when the entire range of the ejecta is measured (e.g. in impact numerical simulations or in very high resolution experiments) and it does not require parts of the data to be cut off. For impact experiments that do not capture the inner and outer regimes, the best approach is to use the simple power-law form, Eq. (6).

Moreover, in our numerical studies we used the same impactor and a constant velocity of 7 km/s. Hermalyn and Schultz (2010) found that the fast ejecta is influenced by the impactor properties so future work is needed to determine the effects of target-impactor density ratio or the impactor velocity on the equation fit.

When comparing the fitting constants found from our numerical simulations with the ones found from laboratory experiments, we notice several discrepancies: Extrapolating from impact experiments, it was expected that  $\mu$  decreases with increasing initial target porosity. Our numerical results show however that an increase in the target porosity, from 10% to 50%, leads to an increase in  $\mu$ , from  $\approx 0.40$  to  $\approx 0.46$  (Fig. 12a). These values are also consistent with the  $\mu$  found from the crater scaling (Section 6.1). We note though that this trend cannot be extrapolated to the no porosity case, where significantly larger  $\mu$  values were found by Prieur et al. (2017).

Also from experiments, it was noted (Cheng et al., 2016) that targets with lower  $\mu$  generally also have a lower  $C_1$ , but our studies showed that  $C_1$  decreases as  $\mu$  increases. The  $k$  parameter value fluctuates as a function of porosity, between 0.37 and 0.45, but there is no clear trend that can be inferred.

Impact experiments into basalt rock ( $\phi_0 \approx \text{few } \%$ ), found  $\mu = 0.55$  and  $C_1 = 1.5$  (Gault et al., 1963; Housen and Holsapple, 2011), impacts into WCB ( $\phi_0 \approx 20\%$ ) found  $\mu = 0.46$  and  $C_1 = 0.18$  (Housen, 1992; Housen and Holsapple, 2011), while impacts into SFA ( $\phi_0 \approx 45\%$ ) found  $\mu = 0.40$  and  $C_1 = 0.55$ . This trend is in contradiction with our results and suggests that it is not straightforward to compare values of  $\mu$  and  $C_1$  determined from experiments for aspecific target material with numerical simulations using idealised material models, as other material properties might be involved and play an important role in the response of real materials (Table 4).

When increasing the coefficient of internal friction, the point source exponent,  $\mu$ , decreases from 0.48 to 0.35 (Fig. 12b). This behaviour of the ejecta and the determined  $\mu$  are again consistent with the crater scaling constants determined in Section 6.1. With increasing  $f$ ,  $C_1$  also increases from 1 to 1.8. While the  $k$  constant remained almost constant when varying the porosity of the target, when increasing coefficient of internal friction,  $k$  slowly decreases from 0.5 for  $f = 0.2$ , to 0.3 for  $f = 1.2$ .

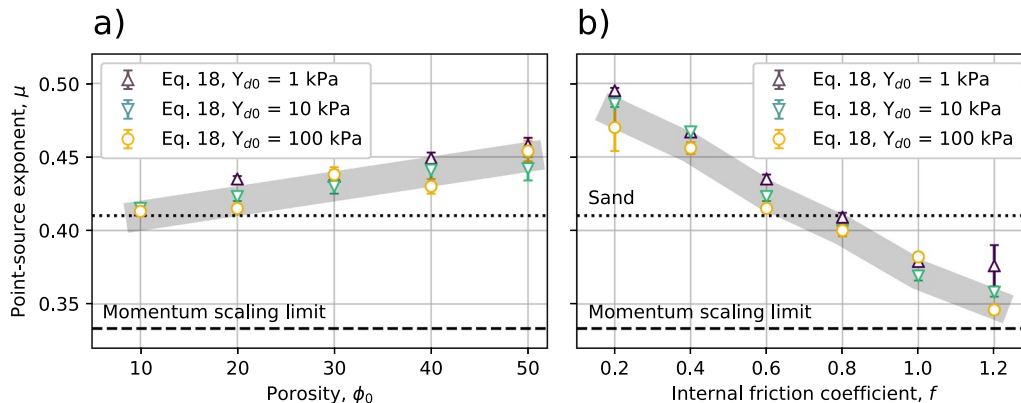


Fig. 12. Results for the point-source exponent,  $\mu$ , obtained by least-square fitting Eq. (18) to the model data.  $\mu$  is determined for three different target cohesions ( $Y_{d0} = 1, 10, 100$  kPa) and plotted as a function of (a) porosity and (b) coefficient of internal friction.



**Table 4**

Impact ejecta scaling parameters for Basalt, WCB, SFA and numerical simulations from this work ( $\phi_0 = 10\%$ – $50\%$  and  $f = 0.6$ ). For all cases  $\nu = 0.4$ ,  $n_1 = 1.2$ ,  $n_2 = 1.0$ .

Target	$\phi_0$	$\mu$	$C_1$	$k$
Basalt <sup>a</sup>	Few %	0.55	1.50	0.3
WCB <sup>b</sup>	20%	0.46	0.18	0.3
SFA <sup>c</sup>	45%	0.40	0.55	0.3
iSALE	10%	0.41	1.58	0.4
iSALE	20%	0.42	1.06	0.4
iSALE	30%	0.43	0.80	0.4
iSALE	40%	0.44	0.58	0.4
iSALE	50%	0.45	0.41	0.4

<sup>a</sup> Housen and Holsapple (2011).

<sup>b</sup> Housen (1992).

<sup>c</sup> Housen and Holsapple (2003).

The fitting constants determined in this section ( $\mu$ ,  $C_1$ ,  $k$ ) can be directly used to infer an analytical value for the amount of momentum transferred from an impact. Inputting the values into Eq. (9), we found  $\beta - 1$  values that are comparable to the simulation data. The analytical values of  $\beta - 1$  are represented by hollow symbols in Fig. 9 and they plot very close to the  $\beta - 1$  values obtained from the numerical simulations, represented by filled symbols. The relative error between the numerical and analytical results is principally derived from uncertainties in the least-squares fitting of Eq. (18) to the numerical data, and ranges between about 5% and 40%.

## 8. Conclusions

We used the iSALE shock physics code to numerically simulate impacts into low-gravity, strength-dominated asteroid surfaces, to quantify the sensitivity of ejecta properties and momentum transfer to variations in asteroid properties. We found that key target material properties, cohesion (of the post-shock target), initial porosity and internal friction coefficient, greatly influence ejecta mass/velocity/launch-position distributions. We found that an increase in porosity or in internal friction leads to lower ejection velocities, while an increase in target cohesion only slows down the last ejecta to leave the crater. This is consistent with the results of recent numerical simulations of ejecta behaviour in gravity-dominated impacts (Luther et al., 2018). As a result, the momentum transferred to the target and carried away by the ejecta is also very sensitive to these material properties.

NASA's DART mission aims to be the first to test a controlled deflection of an asteroid by impact momentum transfer. Our simulation results suggest the cohesion of the target asteroid's surface after passage of the shock wave has the greatest influence on momentum transfer. As the cohesion is decreased the ratio of ejected momentum to impactor momentum  $\beta - 1$  increases;  $\beta - 1$  also increases as the initial porosity and internal friction coefficient of the asteroid surface decrease. Using nominal impactor parameters and reasonable estimates for the material properties of the Didymos binary asteroid, the DART target, the  $\beta$  factor ranged from approximately 2.4 for a cohesion of 10 kPa to approximately 4 for a cohesion of 0.1 kPa. For a tighter constraint on the  $\beta$  value, a more accurate characterisation of the target asteroid is needed and as such, it would be advantageous to survey the target before or after impact. An accurate measurement of the DART impact crater diameter would help constrain the cohesion of the target surface. We also found that the analytical expression for estimating  $\beta$  for a given impact scenario derived by Cheng et al. (2016) is consistent with our numerical simulation results to within  $\approx 10\%$ .

Numerical impact simulations that replicated conditions in three laboratory experiments (Cintala et al., 1999; Hermalyn and Schultz, 2011; Housen and Holsapple, 2011) demonstrate that our approach to quantify ejecta properties is consistent with impact experiments in analog materials. Furthermore, the final crater sizes predicted by our

numerical simulations are consistent with strength-regime crater scaling relationships based on laboratory impact experiments in two asteroid analogous materials: weakly-cemented basalt (WCB) (Housen, 1992) and the Sand Fly/ash (SFA) (Housen and Holsapple, 2003). Widely-used, power-law scaling relationships for estimating both crater size and ejecta behaviour are linked by a target-material-specific parameter,  $\mu$ , known as the velocity exponent. For the same impactor parameters, our numerical simulation results suggest that  $\mu$  is independent of target cohesion and decreases slightly as the initial target porosity increases from 10% to 50%. On the other hand  $\mu$  decreases rapidly with increasing target coefficient of internal friction. This dependence of  $\mu$  on target properties is slightly different to that inferred from impact experiments, but it is consistent with other recent numerical impact simulations (Luther et al., 2018; Prieur et al., 2017; Wünnemann et al., 2016).

Finally, we investigated the self-consistency between the crater size and ejection speed scaling relationships previously derived from the point-source approximation for impacts in the same target material (Holsapple, 1993; Housen and Holsapple, 2011; Housen et al., 1983). Contrary to some previous ejecta studies, we found that for our strength-regime impacts the two relationships do give consistent values of the velocity exponent  $\mu$ , so long as a simple power-law function is used to fit the ejecta data over the radial range  $4a < x < 0.74R$ , where  $a$  is the impactor radius and  $R$  is the final crater rim radius. Alternatively, we proposed a revision to the Housen and Holsapple (2011) ejecta scaling relationship that accounts for the non-power-law behaviour in the coupling zone close to the impact point and provides a good fit to our numerical simulation results over the full radial range of ejecta data  $a < x < R$ . This relationship also leads to consistent  $\mu$  values obtained from ejecta and crater size data in the same target material, but allows a much greater range of ejecta data to be included. The consistency in  $\mu$  values between crater size and ejecta scaling data provides support for applicability of the point-source approximation in impact ejecta scaling.

## Acknowledgements

We gratefully acknowledge the developers of iSALE-2D ([www.isale-code.de](http://www.isale-code.de)), including Kai Wünnemann, Dirk Elbeshausen, Boris Ivanov and Jay Melosh. This work was funded by Science and Technology Facilities Council (STFC) (Grant ST/N000803/1).

## Appendix A. Supplementary data

Supplementary data to this article can be found online at <https://doi.org/10.1016/j.icarus.2019.03.040>.

## References

- Ahrens, T.J., Harris, A.W., 1992. Deflection and fragmentation of near-Earth asteroids. *Nature* 360 (6403), 429–433.
- Amsden, A.A., Ruppel, H.M., Hirt, C.W., 1980. SALE: a simplified ALE computer program for fluid flow at all speeds. In: Tech. Rep. LA-8095, pp. 5176006.
- Anderson, J.L.B., Schultz, P.H., Heineck, J.T., 2003. Asymmetry of ejecta flow during oblique impacts using three-dimensional particle image velocimetry. *J. Geophys. Res. Planets* 108 (E8).
- Belton, M.J.S., Belton, M.J.S., Morgan, T.H., Samarasinha, N.H., Yeomans, D.K., 2004. Mitigation of Hazardous Comets and Asteroids. Cambridge University Press.
- Benck, R.F., Filbey Jr., G.L., Murray Jr., E., 1976. Quasi-static compression stress-strain curves-IV, 2024-t3510 and 6061-t6 aluminum alloys. In: Tech. Rep. Army Ballistic Research Lab, Aberdeen Proving Ground MD.
- Cheng, A.F., Michel, P., Jutzi, M., Rivkin, A.S., Stickle, A., Barnouin, O., Ernst, C., Atchison, J., Pravec, P., Richardson, D.C., 2016. Asteroid impact & deflection assessment mission: kinetic impactor. *Planet. Space Sci.* 121, 27–35.
- Cheng, A.F., Rivkin, A.S., Michel, P., Atchison, J., Barnouin, O., Benner, L., Chabot, N.L., Ernst, C., Fahnestock, E.G., Kueppers, M., Pravec, P., Rainey, E., Richardson, D.C., Stickle, A.M., Thomas, C., 2018. AIDA DART asteroid deflection test: planetary defense and science objectives. *Planet. Space Sci.* 157, 104–115.
- Cintala, M.J., Berthoud, L., Hörz, F., 1999. Ejection-velocity distributions from impacts into coarse-grained sand. *Meteorit. Planet. Sci.* 34 (4), 605–623.
- Collins, G.S., Melosh, H.J., Ivanov, B.A., 2004. Modeling damage and deformation in

- impact simulations. *Meteorit. Planet. Sci.* 39 (2), 217–231.
- Collins, G.S., Melosh, H.J., Wünnemann, K., 2011. Improvements to the epsilon-alpha porous compaction model for simulating impacts into high-porosity solar system objects. *Int. J. Impact Eng.* 38 (6), 434–439.
- Durda, D.D., Bottke, W.F., Enke, B.L., Merline, W.J., Asphaug, E., Richardson, D.C., Leinhardt, Z.M., 2004. The formation of asteroid satellites in large impacts: results from numerical simulations. *Icarus* 170, 243–257.
- Elbeshausen, D., Wünnemann, K., Collins, G.S., 2009. Scaling of oblique impacts in frictional targets: implications for crater size and formation mechanisms. *Icarus* 204 (2), 716–731.
- Fassett, C.I., Minton, D.A., 2013. Impact bombardment of the terrestrial planets and the early history of the Solar System. *Nat. Geosci.* 6 (7), 520–524.
- Gault, D., Shoemaker, E., Moore, H., Aeronautics, U. S. N., Administration, S., Center, A. R., 1963. Spray ejected from the lunar surface by meteoroid impact. In: NASA Technical Note. National Aeronautics and Space Administration.
- Goodman, R., 1989. Introduction to Rock Mechanics. Wiley.
- Greenberg, R., Chapman, C.R., 1983. Asteroids and meteorites: parent bodies and delivered samples. *Icarus* 55 (3), 455–481.
- Hartmann, W.K., 1985. Impact experiments. *Icarus* 63 (1), 69–98.
- Heiken, G.H.V., 1991. Lunar sourcebook - a user's guide to the moon. In: Tech. Rep. Hermaryn, B., Schultz, P.H., 2010. Early-stage ejecta velocity distribution for vertical hypervelocity impacts into sand. *Icarus* 209 (2), 866–870.
- Hermaryn, B., Schultz, P.H., 2011. Time-resolved studies of hypervelocity vertical impacts into porous particulate targets: effects of projectile density on early-time coupling and crater growth. *Icarus* 216 (1), 269–279.
- Holsapple, K.A., 1993. The scaling of impact processes in planetary sciences. *Annu. Rev. Earth Planet. Sci.* 21 (1), 333–373.
- Holsapple, K.A., Housen, K.R., 2012. Momentum transfer in asteroid impacts. I. Theory and scaling. *Icarus* 221 (2), 875–887.
- Holsapple, K.A., Schmidt, R.M., 1982. On the scaling of crater dimensions. II - impact processes. *J. Geophys. Res.* 87, 1849–1870.
- Holsapple, K.A., Schmidt, R.M., 1987. Point source solutions and coupling parameters in cratering mechanics. *J. Geophys. Res. Solid Earth* 92 (B7), 6350–6376.
- Housen, K.R., 1992. Crater ejecta velocities for impacts on rocky bodies. In: Lunar and Planetary Science Conference. vol. 23.
- Housen, K.R., Holsapple, K.A., 2003. Impact cratering on porous asteroids. *Icarus* 163 (1), 102–119.
- Housen, K.R., Holsapple, K.A., 2011. Ejecta from impact craters. *Icarus* 211 (1), 856–875.
- Housen, K.R., Schmidt, R.M., Holsapple, K.A., 1983. Crater ejecta scaling laws: fundamental forms based on dimensional analysis. *J. Geophys. Res. Solid Earth* 88 (B3), 2485–2499.
- Ivanov, B.A., Artemieva, N.A., 2002. Numerical modeling of the formation of large impact craters. In: Special Paper 356: Catastrophic Events and Mass Extinctions: Impacts and Beyond. vol. 356. Geological Society of America, pp. 619–630.
- Ivanov, B.A., Deniem, D., Neukum, G., 1997. Implementation of dynamic strength models into 2D hydrocodes: applications for atmospheric breakup and impact cratering. *Int. J. Impact Eng.* 20 (1), 411–430.
- Ivanov, B.A., Melosh, H.J., Pierazzo, E., 2010. Basin-forming impacts: reconnaissance modeling. *Geol. Soc. Am. Spec. Pap.* 465, 29–49.
- Jacobson, S.A., Scheeres, D.J., 2011. Dynamics of rotationally fissioned asteroids: source of observed small asteroid systems. *Icarus* 214 (1), 161–178.
- Johnson, B., Bowling, J.T., Melosh, J., 2014. Jetting during vertical impacts of spherical projectiles. *Icarus* 238, 13–22.
- Johnson, G.R., Cook, W.H., 1983. A constitutive model and data for metals subjected to large strains, high strain rates and high temperatures. In: Proceedings of the 7th International Symposium on Ballistics, The Hague, pp. 541–547.
- Jutzi, M., Michel, P., 2014. Hypervelocity impacts on asteroids and momentum transfer I. Numerical simulations using porous targets. *Icarus* 229, 247–253.
- Lee, K.L., Seed, H.B., 1967. Drained strength characteristics of sands. *J. Soil Mech. Found. Div.* 93 (6), 117–141.
- Lu, E.T., Love, S.G., 2005. Gravitational tractor for towing asteroids. *Nature* 438 (7065), 177–178.
- Lundborg, N., 1967. The strength-size relation of granite. *Int. J. Rock Mech. Min. Sci. Geomech. Abstr.* 4 (3), 269–272.
- Luther, R., Zhu, M.-H., Collins, G., Wünnemann, K., 2018. Effect of target properties and impact velocity on ejection dynamics and ejecta deposition. *Meteorit. Planet. Sci.* 53 (8), 1705–1732.
- Melosh, H.J., 1989. Impact cratering: a geologic process. In: Oxford Monographs on Geology and Geophysics. Oxford University Press.
- Melosh, H.J., 2007. A hydrocode equation of state for SiO<sub>2</sub>. *Meteoritics & Planetary Science Archives* 42 (12), 2079–2098.
- Melosh, H.J., Nemchinov, I.V., Zetzer, Y.I., 1994. Non-nuclear Strategies for Deflecting Comets and Asteroids. pp. 1111–1132.
- Michel, P., 2013. Physical properties of near-earth objects that inform mitigation. *Acta Astronaut.* 90 (1), 6–13.
- Michel, P., Cheng, A., Küppers, M., Pravec, P., Blum, J., Delbo, M., Green, S., Rosenblatt, P., Tsiganis, K., Vincent, J., Biele, J., Ciarletti, V., Hérique, A., Ulamec, S., Carnelli, I., Galvez, A., Benner, L., Naidu, S., Barnouin, O., Richardson, D., Rivkin, A., Scheirich, P., Moskovitz, N., Thirouin, A., Schwartz, S., Campo Bagatin, A., Yu, Y., 2016. Science case for the asteroid impact mission (AIM): a component of the asteroid impact & deflection assessment (AIDA) mission. *Adv. Space Res.* 57 (12), 2529–2547.
- Michel, P., Kueppers, M., Sierks, H., Carnelli, I., Cheng, A.F., Mellab, K., Granvik, M., Kestilä, A., Kohout, T., Muinonen, K., Näsälä, A., Penttilä, A., Tikka, T., Tortora, P., Ciarletti, V., Hérique, A., Murdoch, N., Asphaug, E., Rivkin, A., Barnouin, O., Bagatin, A.C., Pravec, P., Richardson, D.C., Schwartz, S.R., Tsiganis, K., Ulamec, S., Karatekin, O., 2018. European component of the AIDA mission to a binary asteroid: characterization and interpretation of the impact of the DART mission. *Adv. Space Res.* 62 (8), 2261–2272.
- Murdoch, N., Hempel, S., Pou, L., Cadu, A., Garcia, R.F., Mimoun, D., Margerin, L., Karatekin, O., 2017. Probing the internal structure of the asteroid Didymos with a passive seismic investigation. *Planet. Space Sci.* 144, 89–105.
- Oberbeck, V.R., 1975. The role of ballistic erosion and sedimentation in lunar stratigraphy. *Rev. Geophys.* 13 (2), 337–362.
- Pierazzo, E., Artemieva, N., Asphaug, E., Baldwin, E.C., Cazamias, J., Coker, R., Collins, G.S., Crawford, D.A., Davison, T., Elbeshausen, D., Holsapple, K.A., Housen, K.R., Korycansky, D.G., Wünnemann, K., 2008. Validation of numerical codes for impact and explosion cratering: impacts on strengthless and metal targets. *Meteorit. Planet. Sci.* 43 (12), 1917–1938.
- Prieur, N.C., Rolf, T., Luther, R., Wünnemann, K., Xiao, Z., Werner, S.C., 2017. The effect of target properties on transient crater scaling for simple craters. *J. Geophys. Res. Planets* 122 (8), 2017JE005283.
- Scheirich, P., Pravec, P., 2009. Modeling of lightcurves of binary asteroids. *Icarus* 200 (2), 531–547.
- Schmidt, R.M., 1980. Meteor Crater: Energy of Formation - Implications of Centrifuge Scaling. vol. 11. pp. 2099–2128.
- Schmidt, R.M., Holsapple, K.A., 1982. Estimates of crater size for large-body impact: gravity-scaling results. *Geol. Soc. Am. Spec. Pap.* 190, 93–102.
- Schultz, P.H., 1988. Cratering on Mercury - a relook. In: Mercury. University of Arizona Press, pp. 274–335.
- Schultz, P.H., 1992. Atmospheric effects on cratering efficiency. *J. Geophys. Res. Planets* 97 (E1), 975–1005.
- Schultz, P.H., Mendenhall, M.H., 1979. On the Formation of Basin Secondary Craters by Ejecta Complexes. vol. 10. pp. 1078–1080.
- Shafer, P.B., Garcia, D.M., Scammon, J.R., Snell, C., Stellingwerf, F.R., Remo, J., Managan, R., Rosenkilde, E.C., 1994. The Coupling of Energy to Asteroids and Comets. vol. 1. pp. 955.
- Shoemaker, E.M., Gault, D.E., Moore, H.J., Lugn, R.V., 1963. Hypervelocity impact of steel into coconino sandstone. *Am. J. Sci.* 261 (7), 668–682.
- Stickler, A.M., Atchison, J.A., Barnouin, O.S., Cheng, A.F., Crawford, D.A., Ernst, C.M., Fletcher, Z., Rivkin, A.S., 2015. Modeling momentum transfer from kinetic impacts: implications for redirecting asteroids. *Procedia Eng.* 103, 577–584.
- Su, S.-Y., 1990. The velocity distribution of collisional fragments and its effect on future space debris environment. *Adv. Space Res.* 10 (3–4), 389–392.
- Syal, M.B., Owen, J.M., Miller, P.L., 2016. Deflection by kinetic impact: sensitivity to asteroidal properties. *Icarus* 269, 50–61.
- Tillotson, H.J., 1962. Metallic equations of state for hypervelocity impact. In: General Atomic Report GA-3216, pp. 141.
- Tsuji, S., Arakawa, M., Suzuki, A.I., Yasui, M., 2015. Ejecta velocity distribution of impact craters formed on quartz sand: effect of projectile density on crater scaling law. *Icarus* 262, 79–92.
- Walsh, K.J., Richardson, D.C., Michel, P., 2008. Rotational breakup as the origin of small binary asteroids. *Nature* 454, 188.
- Walsh, K.J., Richardson, D.C., Michel, P., 2012. Spin-up of rubble-pile asteroids: disruption, satellite formation, and equilibrium shapes. *Icarus* 220 (2), 514–529.
- Wünnemann, K., Collins, G.S., Melosh, H.J., 2006. A strain-based porosity model for use in hydrocode simulations of impacts and implications for transient crater growth in porous targets. *Icarus* 180 (2), 514–527.
- Wünnemann, K., Zhu, M.-H., Stöffler, D., 2016. Impacts into quartz sand: crater formation, shock metamorphism, and ejecta distribution in laboratory experiments and numerical models. *Meteorit. Planet. Sci.* 51 (10), 1762–1794.
- Yamamoto, S., Okabe, N., Kadono, T., Sugita, S., Matsui, T., 2005. Measurements of Ejecta Velocity Distribution by a High-Speed Video Camera. vol. 36.
- Yamamoto, S., Hasegawa, S., Suzuki, A.I., Matsunaga, T., 2017. Impact velocity dependence of transient cratering growth. *J. Geophys. Res. Planets* 122 (5), 1077–1089.
- Yang, W., Ahrens, T.J., 1995. Impact jetting of geological materials. *Icarus* 116 (2), 269–274.
- Yeomans, D.K., Barriot, J.-P., Dunham, D.W., Farquhar, R.W., Giorgini, J.D., Helfrich, C.E., Konopliv, A.S., McAdams, J.V., Miller, J.K., Owen Jr., W.M., Scheeres, D.J., Synnott, S.P., Williams, B.G., 1997. Estimating the mass of asteroid 253 Mathilde from tracking data during the NEAR flyby. *Science* 278, 2106.